Modeling and Analyzing MHD Waves in a Sheared-Flow Z-Pinch Plasma

Nicolas Castriotta

A thesis
submitted in partial fulfillment of the
requirements for the degree of

Master of Science

University of Washington

2024

Reading Committee:
Uri Shumlak

Justin Little

Program Authorized to Offer Degree:

Aeronautics and Astronautics

University of Washington

Abstract

Modeling and Analyzing MHD Waves in a Sheared-Flow Z-Pinch Plasma

Nicolas Castriotta

Chair of the Supervisory Committee:

Uri Shumlak

Aeronautics and Astronautics

The ZaP-HD Z-Pinch device is a modification of the Z-Pinch nuclear fusion device using a sheared plasma flow to promote stability and reduce the traditional downfalls of the highly unstable Z-Pinch design. Z-Pinches are confined by generating their own magnetic field that manifests tangentially around an axial “Z”-facing current. The plasma is then compressed to high densities and temperatures where it would ultimately lead to fusion in a commercial device. Inherent to plasma are waveforms that are created from the microscopic perturbations of particles and electromagnetic fields within its medium. Unlike simpler electrostatic environments both theoretical or in real-world cases like grid-acceleration ion thrusters, however, magnetic fields create vast anisotropies that cause a “zoo” of waves to appear within the plasma. These waves can cause nonlinear/higher order effects when coupled with particle energy exchanges that can lead to significant instabilities. Despite this, wave phenomena and their resonant interactions with the plasma are helpful for applications like heating to fusion temperature or understanding radiation transmission. To best take advantage of these useful properties, it is best to get an accurate picture of the wave behavior within ZaP-HD that is tailored to its specific geometry, plasma energy, and field strength. The problem is

that when analyzing the wide spectrum of possible wave modes, the “zoo” is vast. Even with just oscillatory modes this is an issue and it gets even more complicated to accurately predict and experimentally analyze when the above mentioned instabilities are introduced. Therefore, a baseline model that starts from and approximates a subsection of the whole plasma wave spectrum without these instabilities is useful. It can serve as a spring-board for further spectral sub-regions and higher-order effects while ensuring accuracy for the many interwoven components of the whole spectrum. This baseline model uses observable data (like magnetic field, density, and flow velocity) within ZaP-HD’s cylindrical fusion plasma environment and predicts the low frequency magnetohydrodynamic (MHD) range. The iteration process then begins with with frequency analysis methods such as cross-correlation and Fourier analysis to compare with the model and check for differences in results. All experimental data is retrieved using probes positioned within the main assembly region of ZaP-HD where the fusion process occurs.

TABLE OF CONTENTS

Page

List of Figures iii

List of Tables viii

Chapter 1: Introduction 1
- 1.1 Nuclear Fusion History and Basics 1
- 1.2 The Z-Pinch Configuration 3
- 1.3 Instabilities in a Static Z-pinch 4
- 1.4 Sheared-Flow Stabilization 6
- 1.5 Motivation and Applications for Analyzing Plasma Waves 7

Chapter 2: The ZaP-HD Flow Z-Pinch Experiment 9
- 2.1 ZaP-HD Device Parameters and Sheared-Flow Pinch Formation 9
- 2.2 Magnetic Field Diagnostic Setup and Data Collection 12
- 2.3 Magnetic Field Probe Theory and ZaP-HD Stability 13
- 2.4 ZaP-HD Applications 17

Chapter 3: Predictive Model for Waveforms 20
- 3.1 Goals and Methodology 20
- 3.2 MHD Plasma Wave Basics 20
- 3.3 Hain-Lüst Equation 23
- 3.4 Singularities and Plasma Profile Assumptions 26
- 3.5 Doppler Shift Correction 27
- 3.6 Alfvén Wave Behavior and Predicted Results 30
- 3.7 Magnetosonic Wave Behavior and Predicted Results 31
- 3.8 Turning Point Frequencies 35

3.9 Prediction Model Analysis Summary 35

Chapter 4: Frequency Analysis of Magnetic Field Probes 39
4.1 Motivation for Analysis and Correlation Basics 39
4.2 Using Cross-Correlation Analysis with ZaP-HD Probe Limitations 40
4.3 Azimuthal Cross-Correlation Analysis Results and Prediction Comparison . . 41
4.4 Axial Cross-Correlation Analysis Results and Prediction Comparison 46

Chapter 5: Investigating Adjustments to the Model 49
5.1 Overview and Non-Quantified Adjustments 49
5.2 Ampere's Law Approximation Adjustment 49
5.3 Pressure and Density Profile Adjustment 50
5.4 Doppler Shift and Velocity Profile Adjustment 50
5.5 Adjustment Summary and Best Solution Suggestion 53

Chapter 6: Conclusion 56
6.1 Research Summary 56
6.2 Future Work 56

LIST OF FIGURES

Figure Number Page

1.1 This is a simple representation of a static z-pinch's confinement mechanism. It shows how a self-generated magnetic field holds and compresses the current it surrounds using the Lorentz force. This compression will allow the plasma to reach thermonuclear temperatures needed for adequate fusion to be possible. [1] 4

1.2 The left image illustrates the typical behavior in the $m = 0$ sausage mode while the right image shows the typical behavior of the $m = 1$ kink mode. It is shown how the magnetic field can distort in the instability region to reinforce the effect and lead to a feedback loop until confinement fails. [2] . . 5

2.1 This image is a diagram of the ZaP-HD device. It illustrates the two-segment design with the approximately 41 inch accelerator region leading to the approximately 21 inch assembly/compression region. The accelerator region contains three electrodes: outer, middle, and inner. The plasma "snowplow" traverses between the middle and inner electrode before it hits the nosecone. In the assembly region, the plasma connects between the outer electrode and the inner electrode nosecone. The magnetic probes within the assembly region are installed at 5 cm intervals. [3] 10

2.2 This image demonstrates a simplified version of the formation of the sheared-flow z-pinch plasma. Image (a) shows the initial introduction of hydrogen gas into the acceleration region of the axial chamber. After this, the gas begins to expand and fill the chamber as depicted in image (b). The capacitors are then charged and engaged, establishing a high potential across the electrodes that ionizes the gas between them (c). The plasma will then generate its own magnetic field as the electric field creates a current facing towards the inner electrode, causing the Lorentz force to push it down the length of the chamber (d). Once the acceleration terminus is reached, the plasma detaches and begins re-combining in a "zipper" fashion in the assembly region (e). A z-pinch is then formed with the sheared flow plasma along the length of the assembly region (f). [4] 11

2.3 Digitized magnetic field readings from the P_{30} probe array. Note the 8 azimuthal readings at 45 degrees equally spaced from each other. As stated earlier, there are 4 positions at 15 cm intervals where the 8-probe array is utilized. Due to the higher amount of azimuthal probes affording a higher number of data points, these locations were chosen for the analysis for radial-propagating wave behavior. 14

2.4 Digitized magnetic field readings from the P_{25} probe array. Note the 4 azimuthal readings at 90 degrees equally spaced from each other. Every remaining probe array not at the 15 cm intervals contain this 4-probe array. This difference between the probe counts contributes to a limit on the analysis for axial-propagating wave behavior that will be discussed in more detail later. . 15

2.5 Illustration of the normalized $m = 1$ mode for positions P_{25} and P_{30} within the assembly region. This gives an idea of the length of time known as the "quiescent" period lasting from around 40 μs to 80 μs where there is low incidence of the MHD modes that lead to z-pinch failure. Once this period passes around 100 μs, however, these modes start to reappear and cause the stability of the pinch to fail and the pulse to end. 16

2.6 A simplified representation of how a specifically sheared-flow z-pinch fusion thruster would operate. Unlike the reactor design, however, it has a diffusing outer electrode for improved performance. A direct energy converter is also shown that greatly benefits the efficiency of the thruster. This direct energy converter modifies the closed nosecone design present within ZaP-HD currently. [5] 18

3.1 Depiction of a diffuse cylindrical plasma of radius a where both an azimuthal and radial component magnetic fields are present. However, for this analysis, the radial magnetic field component will be redundant to the final result. The symbol μ is representative of the ratio between the azimuthal and radial fields. 24

3.2 Illustration of the parabolic density profile with the 7 discrete radial locations of 0.1 mm, 0.5 mm, 1 mm, 1.5 mm, 2.0 mm, 2.5 mm, and 2.9 mm. The mass density begins at its peak of 1.67×10^{-4}kg/m^{-3} at the center of the plasma and tapers off to 0 at the edge. 0 mm and 3 mm away from the plasma center were not chosen to avoid singularities in the model. 28

3.3 Illustration of the parabolic pressure profile with an identical appearance to the density profile and at the same 7 radial locations. Again, 0 mm and 3 mm away from the center are avoided to stop singularities from appearing. Peak pressure was related to density by the state function $P = nk_bT$. 29

3.4 A visual for helping show the direction of travel of Alfvén waves relative to other plasma parameters. These parameters are: the equilibrium magnetic field (B) which is parallel to propagation, the perturbed magnetic field (B') which is perpendicular to propagation, and the perturbed velocity (v') which is perpendicular to propagation. [6][7] 30

3.5 This predicted behavior of the Alfvén sub-spectra ($\omega_A(r)^2$) yields the following results for the 8 azimuthal locations within ZaP-HD at the 7 discrete radial locations mentioned earlier. It shows a strong correlation between frequency and radius owing to the strengthening magnetic field and shrinking density at higher radii shown an Eq. 3.37. 32

3.6 This visualizes the perpendicular propagation of a magnetosonic wave relative to other plasma parameters. Compared to Alfvén wave propagation, the equilibrium magnetic field (B) is now shown perpendicular to magnetosonic propagation. [6][7] 33

3.7 Results the following results of the slow mangetosonic sub-spectra ($\omega_S(r)^2$) for the 8 azimuthal locations within ZaP-HD at the 7 discrete radial locations mentioned earlier. As mentioned previously, the frequency range is less than but close to the Alfvén range which is expected. However, the radial correlation between radius and frequency is not as strong for slow magnetosonic waves due to its more complex dependence on the magnetic field and density/pressure profiles. 34

3.8 A visual for helping understand where the turning point frequencies are situated between the other other continuous essential sub-spectra. The slow turning point frequency exists between the domains of the slow magnetosonic and Alfvén sub-spectra. The fast turning point frequency does the same for the Alfvén and fast magnetosonic sub-spectra. However, as stated earlier, the fast magnetosonic domain is entirely at infinity within this model based on Hain-Lüst. [8] 36

3.9 The results for the slow turning point frequency ($\omega_{s0}(r)^2$) illustrate how the frequency values look similar to the slow magnetosonic sub-spectra center-of-plasma behavior as it approaches r = 0 mm. There exists some saturation artifact at the 0 degrees location of unknown origin that does not appear in any of the other azimuthal readings. 37

3.10 Contrasting with the slow turning point frequency, the fast turning point frequency ($\omega_{f0}(r)^2$) shows a quickly increasing asymptotic progression to infinity as it approaches lower radii with r = 0.1 mm being significantly higher than other locations further out. This matches it with the constantly infinity fast magnetosonic sub-spectra. The drastically different appearance between the slow and fast turning point frequencies can be explained by viewing Eq. 3.39 an seeing the plus or minus sign differentiating the two. Just changing the minus sign to a plus sign for the fast turning point frequency leads to this behavior. 38

4.1 This is a test correlation analysis demonstrating the method. The top plot was acquired from delaying a non-noisy signal (sinc(x) function) with the same signal by a distance of $\frac{33\pi}{2}$ and correlating it with the original unaltered signal with a spike at 0. It is shown that the analysis has a correlation spike right at the delay amount. The lower plot was acquired from applying a random noise on top of the two clean superimposed sinc(x) signals to prove the cross-correlation function's effectiveness in noisier circumstances. 42

4.2 Shows the averaged data at P25 using the *smoothdata* function on the *lowess* setting. It is subsequently subtracted from the raw dataset. The function setting *lowess* creates a smoothed version of the raw data through a linear regression over the time window. This method creates less discontinuities than with a moving average. This probe average represents the low frequency behavior that the cross-correlation will detect and skew the results downward. 43

4.3 Shows the averaged data at P30 using the *smoothdata* function on the *lowess* setting. It is then subtracted from the raw output. This same method was done at this location to avoid discontinuities from a moving average smoothing method. This represents the same low frequency behavior but with an 8 azimuthal probe array. 44

4.4 Illustrates the correlation between the magnetic field probes located at azimuthal positions in P30 are shown. The maximum in the graphs were found and the times (period) were inverted to find a frequency. Some of the cross-correlations (between 135 and 180 degrees) revealed maximums that were not close to zero that skewed the average. Despite that, the same takeaway still applies whether these are included or not in the average Alfvén frequency: there is a noticeable difference in predicted results from model and results taken from the frequency analysis. 45

4.5 In this figure, the correlation between the magnetic field probes located at axial positions between P25 and P30 at zero degrees is shown. As in the Alfvén case, the maximum in the graph was found and the period was inverted to find a frequency. Despite the analysis being performed at only a single radial location, it shows a similar result from the Alfvén frequency results: that the axially propagating slow magnetosonic wave frequency does not match with that found in the predictive model. 47

4.6 In this figure, the magnetic field data at P30 and 0 degrees is inputted into the *FFT* fast Fourier transform function in MATLAB to output a frequency range at this probe location. This result was then compared with the cross-correlation result to corroborate the findings found that showed the discrepancy with the predictive model for slow mangetosonic waves. 48

5.1 In this figure, the Alfvén sub-spectra is modified from the initial Ampere's Law profile approximation to the deviated faster scaling relation ship of $B \propto r^{1.5}$. This change to the radial magnetic field behavior causes a sizable shift from the original predicted results and lowers them by a factor of about 100. . . . 51

5.2 In this figure, the density profile was increased to as high as a $\rho \propto 1/r^6$ drop-off in order to emphasize the effect it would have on the model. Ultimately, it was a small change when comparing it to the effect of the magnetic field profile adjustment with the outputted frequencies being in the same 10^7 and 10^8 rad/s range as the original prediction. This was performed on the Alfvén sub-spectra. 52

5.3 In this figure, wavenumber multiplied by the velocity profile at the given radial location within the plasma is amplified from k = 1 to k = 1000. This change is done on the slow magnetosonic sub-spectra. The change is not easily noticed with the frequencies appearing in the same range as the original predictions. There is also the issue of having negative frequency values that don't make sense physically. 54

5.4 In this figure, the velocity profile is modified from its original linear profile to a square root relationship. This was performed on the slow magnetosonic sub-spectra. The effects of this alteration to the shape of the velocity gradient are small with the original 10^7 to 10^8 rad/s range of frequencies appearing. This can be explained partially by the limit of a shift in the velocity profile that doesn't change the magnitudes of center or surface values. 55

LIST OF TABLES

Table Number Page

2.1 ZaP-HD plasma parameters 12

DEDICATION

To those I care about who supported me through this.

Chapter 1

INTRODUCTION

1.1 Nuclear Fusion History and Basics

Within the nucleus of an atom, there exists energetically bound protons and neutrons. By using the mass defect established by

$$m_{defect} = [(Zm_{proton} + Nm_{neutron}) - m_{atom}] \tag{1.1}$$

and Einstein's well known equation for mass-energy equivalence, you come to the remarkable conclusion that nuclei weigh less than the sum of their parts and will release this mass as converted energy. This result is by itself quite tremendous but the full implications of such a phenomenon would not be seized upon until after the discovery of the nuclear fission of uranium by Otto Hahn and Lise Meitner in 1938 [9]. This new energy source could be unlocked through two distinct paths: the splitting of heavy elements known as fission, and the combining of light elements known as fusion. To briefly mention fission, the first functioning reactor prototype, called *Chicago Pile-1*, was completed by Enrico Fermi and his team of scientists in 1942 which began the modern nuclear energy epoch we have today. Fusion, on the other hand, has had a longer and more arduous history. While originally researched in secret during the early Cold War, it was revealed to the public in 1958 at an atomic energy conference in Geneva [10]. This kick-started the current journey of finding a way to achieve a net-energy gain from the process that powers the Sun.

There are many upsides to choosing fusion over fission with notable examples being: renewable fuel and a higher energy output density. However, due to the incredibly high energy requirements for getting fusion to occur as described by the Coulomb barrier where

Z_1 and Z_2 are particle charge state and r_n is interaction radius,

$$E_{peak} = \frac{Z_1 Z_2}{4\pi\epsilon_0}\frac{e^2}{r_n} \tag{1.2}$$

a collection of nuclei need to be heated to millions of degrees in order to actually overcome the Coulomb barrier and fuse consistently enough for above negligible power output. This heating causes the atoms to ionize and form a plasma that must be contained for fusion to occur effectively. In order to access the energy of fusion with the least resistance from confining an astronomically hot plasma, the deuterium-tritium fusion reaction has been explored as the most likely candidate to reach this goal. As shown below,

$$\mathrm{D} + \mathrm{T} \rightarrow \mathrm{n} + \alpha + 17.6\,\mathrm{MeV} \tag{1.3}$$

this reaction has the highest cross section (“probability”) for fusion to occur at comparatively low temperatures around 10-20 keV. Even with this reaction being the easiest to catalyze, there are many difficulties with achieving such a result and thus many strategies have been tried. Most man-made reactor concepts fall under two main categories: inertial confinement and magnetic confinement.

Magnetic confinement, the focus of this paper, is achieved through the use of the Lorentz $\mathbf{j}\times\mathbf{B}$ force trapping charged particles of the plasma near magnetic field lines to counteract the pressure. If the various radiation losses, transport losses, and instabilities can be minimized by a magnetic system while simultaneously maintaining thermonuclear temperatures (in this example 20 keV), the Lawson Criterion shown as

$$n\tau \geq 10^{14}\frac{\mathrm{s}}{\mathrm{cm}^2} \tag{1.4}$$

can be reached to achieve a self-sustaining net-positive reaction [11]. While the most well known magnetic confinement reactors include the geometrically and architecturally complex tokamak and stellarator, a simple and effective alternative for fusion known as the z-pinch will be the focus of this report.

1.2 The Z-Pinch Configuration

The z-pinch was one of the first attempts at thermonuclear fusion with notable early tests dating back to the 1950s [12]. Unlike other reactors' reliance on large electromagnets to generate the confining magnetic field, the z-pinch magnetic field is self-generated. As the name suggests, z-pinches involve sending a current along the "z" axis which generally means in a linear path along the length of the reactor. Since currents generate magnetic fields inherently, this relationship interacts to create the confining and compressing Lorentz force as described by the 1D radial MHD relationship

$$\frac{dp}{dr} = -J_z B_\theta \tag{1.5}$$

with an axial-only current (described by J_z) generating an orthogonal magnetic field (described by B_θ) in the theta-only direction. When combined with Ampere's Law in a 1D radial geometry

$$\frac{1}{r}\frac{d}{dr}(rB_\theta) = \mu_0 J_z \tag{1.6}$$

you acquire the z-pinch confinement relationship between plasma pressure (described by p) and magnetic force.

$$\frac{d}{dr}\left(p + \frac{B_\theta^2}{2\mu_0}\right) = \frac{B_\theta^2}{\mu_0 r} \tag{1.7}$$

The physical representation of this relationship is depicted above in Figure 1.1. Plasma pressure in most cases can be reasonably approximated using an ideal gas state equation. However, since ion and electron temperatures have the potential to exist outside an equilibrium with each other, they're unique contributions should be considered additive. The density of z-pinch devices is also notably high compared to other reactor configurations [5].

Another useful benefit of the z-pinch is the fact it confines plasma at a unity beta. This term represents the ratio of the average plasma pressure to magnetic pressure at the conducting wall radius as shown here:

$$<\beta>= \frac{<p>}{B_\theta^2(r_w)/(2\mu_0)} = 1 \tag{1.8}$$

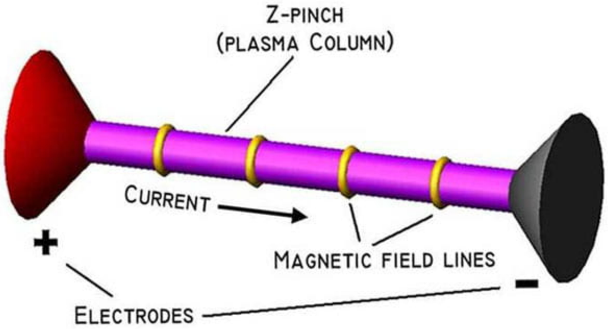

Figure 1.1: This is a simple representation of a static z-pinch's confinement mechanism. It shows how a self-generated magnetic field holds and compresses the current it surrounds using the Lorentz force. This compression will allow the plasma to reach thermonuclear temperatures needed for adequate fusion to be possible. [1]

It is a useful term for showcasing the ideal confinement capabilities of a z-pinch compared to a the lower beta values in a tokamak or a stellarator. However, despite the z-pinch's theoretical advantages over other confinement mechanisms, there are issues with the stability of the simple/static z-pinch that cause confinement to fail quickly.

1.3 Instabilities in a Static Z-pinch

The static z-pinch is highly susceptible to catastrophic macroscopic instabilities known as "sausage" and "kink" instabilities. These correspond to the azimuthal mode numbers $m = 0$ and $m = 1$ respectively [13]. This will destabilize the plasma's coherency and cause a collapse in confinement. As stated by their informal titles, the plasma's behavior follows the shape of a sausage end and a kink. Both of these circumstances are detailed above in Figure 1.2. These instabilities are cascading and will continue to worsen until the plasma confinement fails due to the self-generating magnetic field becoming de-stabilized and strengthening the instability. In the sausage case a simple shrinkage in the plasma radius will cause the magnetic field to locally strengthen and continue the shrinkage. In the kink case, any jostling outside of

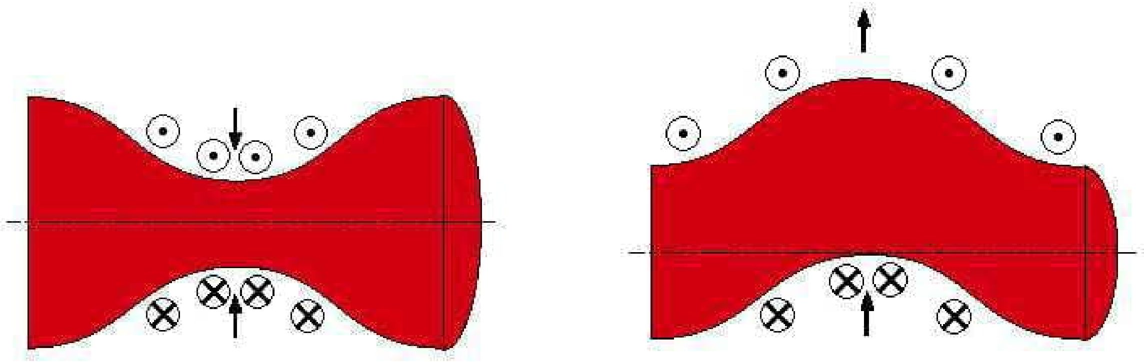

Figure 1.2: The left image illustrates the typical behavior in the $m = 0$ sausage mode while the right image shows the typical behavior of the $m = 1$ kink mode. It is shown how the magnetic field can distort in the instability region to reinforce the effect and lead to a feedback loop until confinement fails. [2]

the linear axis by wave modes or otherwise will cause the magnetic field to weaken in the direction of the kink and strengthen on the bent edge [11]. There have been many attempts to alleviate these devastating instability modes from occurring as they are they are more or less causing all the problems.

One such method has been the usage of an axial magnetic field B_z in order to create a shear that reduces the instabilities. However, it creates open ends to the magnetic field lines that leads to losses and requires the expensive addition of EM coils for generating the field [14]. Another possible method involves using conducting walls close the plasma that encourages “image” currents to form that oppose the creation of the $m = 0$ and $m = 1$ modes [14]. This method, however, is also fraught with issues mostly involving the high energy fluxes from a fusion temperature plasma causing a critical failure in material integrity. If we look at the $m = 0$ mode specifically, there is an effective method for reducing instability through the control of the radial pressure profile. If you can ensure the slope of the radial profile is gradual enough, you can avoid the growth of a sausage instability. The profile can be shown as

$$\frac{d(\ln p)}{d(\ln r)} \leq \frac{4\gamma}{2+\gamma\beta} \tag{1.9}$$

where beta represents the same ratio stated earlier and gamma represents the ratio of specific heats $\gamma = \frac{C_p}{C_v}$ [15][16]. This method, however, will not mitigate the kink instability [17].

1.4 Sheared-Flow Stabilization

Despite the shortcomings of the axial magnetic field and conducting wall methods, all hope is not lost. There is a third method that can be used to effectively reduce the buildup of these instabilities without sacrificing cost or complexity and without having to work around the high energies of a fusion plasma. This method, known as sheared-flow stabilization, will be discussed as it is the foundational innovation used for ZaP-HD and therefore the work in this paper. It has been determined that the $m = 1$ kink mode can be stabilized by having an axial (non-uniform) sheared-flow of plasma simultaneous to the formation of the z-pinch. This axially coherent pinch will last through many more plasma timescales (like a radial acoustic wave propagation time) than a static environment. However, in order to find a threshold where the sheared flow reduces the kink mode, the lack of axisymmetry of the kink mode precludes use of analytical derivations. Therefore, numerical analysis is done starting from a linearized MHD equation set. At the conclusion of this method on a z-pinch, the relationship

$$\frac{dv_z}{dr} \geq 0.1kV_A \tag{1.10}$$

where k is the axial instability wave-number and V_A is the Alfvén speed shows the necessary threshold [15]. What complements this advantage is how the axial flow does not disrupt the unity beta relationship of a z-pinch [14]. On top of that, the necessity of radial profile control may be reduced by the use of a sheared flow as it seems capable of diminishing the sausage mode simultaneously to the kink mode [15].

1.5 Motivation and Applications for Analyzing Plasma Waves

Plasma waves provide insight into the fundamental inner workings of a plasma's behavior. For example, local perturbations of charge carriers (like electrons) result in a fundamental oscillation frequency commonly known as the "plasma" frequency. This property, shown as

$$\omega_{pe} = \sqrt{\frac{n_e e^2}{m_e \epsilon_0}} \tag{1.11}$$

where n_e represents electron density, e represents elementary charge, m_e electron mass, and ϵ_0 the free space permittivity, can be tied to the Debye length. This measurement, which can be calculated as

$$\lambda_{De} = \frac{v_e}{\sqrt{2}\omega_{pe}} \tag{1.12}$$

where v_e represents thermal electron speed in a Maxwellian particle distribution, is partly influenced by this fundamental plasma frequency and plays an important role in understanding how the electric fields of plasma particles behave in the presence of other particles. However, despite the insight gained from just including electrostatic behavior, these represent a small part of the vast "zoo" that arises when a magnetic field is present. This results from the large inhomogeneities that result from the field gradients guiding the manifestation of waveforms. [18].

To briefly describe the applications for the study of waveforms, it has usefulness in a variety of fields ranging from ionospheric physics, astrophysics, fusion plasmas, and laser-produced plasmas. The ionosphere represents an obstacle for things like radio transmission with whistler waves being a notable discovery in the 20th century during the early uses of radio communication. In the case of astrophysics, plasma waves are important for understanding energy and momentum propagation throughout the universe through wave interactions with particle distributions. Laser produced plasmas will arise in the process of inertial confinement fusion where extreme nonlinearity can result in rampant sideband and shock waves. Despite not always being magnetized, these plasmas have steep gradients that encourage highly complex behavior outside the scope of this paper [18].

More related to the topic of this paper, magnetized fusion plasmas can be affected and manipulated by the presence of these waves. As discussed earlier with z-pinch shortcomings, plasma waves influence the behavior of macro scale MHD instabilities while also catalyzing microscopic mode growth. Wave-particle interactions have been taken advantage of to develop the concept of wave heating for a plasma to achieve thermonuclear and eventually ignition temperatures; it involves using the inherit capabilities of waves to transfer energy back and forth between the plasmas particles and the various wave modes [18].

Chapter 2

THE ZAP-HD FLOW Z-PINCH EXPERIMENT

2.1 ZaP-HD Device Parameters and Sheared-Flow Pinch Formation

ZaP-HD, as shown in Figure 2.1, creates its sheared flow through a two-segment process known as an acceleration region upstream and an assembly region downstream [19][20][14]. In the coaxial accelerator region, neutral hydrogen gas is pumped into the chamber to be ionized by gas breakdown between two capacitor-charged electrodes typically carrying a potential of about 7-9 kV (though these values can differ depending on experimental parameters). Once this initial plasma formation experiences the Lorentz force, it will begin accelerating between the middle and inner electrodes in a "snowplow" configuration until it reaches the end of the inner electrode (a nosecone is placed at this terminus) [19][14][20]. Once the plasma reaches the end of the accelerator region, it will detach itself from the middle electrode and re-connect along the central axis of the chamber from the outer electrode to the nosecone [19][20][14]. Adiabatic compression will commence as the pinch is formed from the $\mathbf{j} \times \mathbf{B}$ force shown by the relationship

$$\frac{T_2}{T_1} = \left(\frac{a_2}{a_1}\right)^{-2(\gamma-1)} \left(\frac{N_2}{N_1}\right)^{\gamma-1} \tag{2.1}$$

where T represents plasma temperature, a the plasma radius, γ the ratio of specific heats, and N ion density[17][14][13]. Once thermonuclear temperatures are achieved, the fusion process (occurring at low intensity in this device) then carries forward as it would in a static environment but now with the added benefit of the sheared flow. This whole process takes about 100 microseconds before the pinch dissipates. Table 2.1 lists general performance capabilities of ZaP-HD with regards to metrics like current and density [11][21]. For specifics

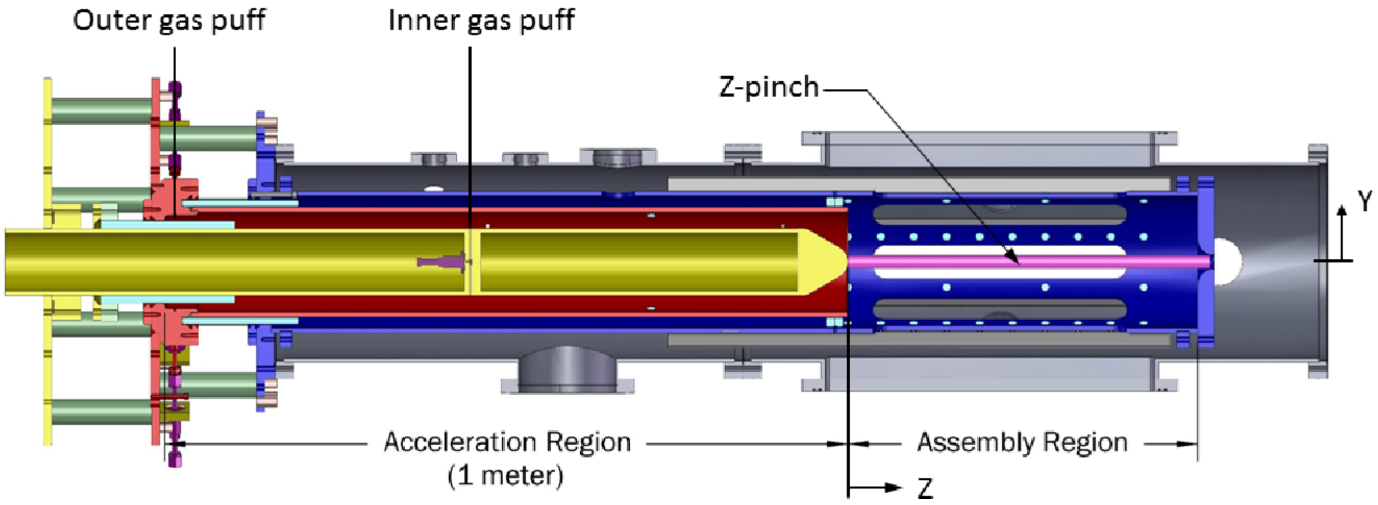

Figure 2.1: This image is a diagram of the ZaP-HD device. It illustrates the two-segment design with the approximately 41 inch accelerator region leading to the approximately 21 inch assembly/compression region. The accelerator region contains three electrodes: outer, middle, and inner. The plasma “snowplow” traverses between the middle and inner electrode before it hits the nosecone. In the assembly region, the plasma connects between the outer electrode and the inner electrode nosecone. The magnetic probes within the assembly region are installed at 5 cm intervals. [3]

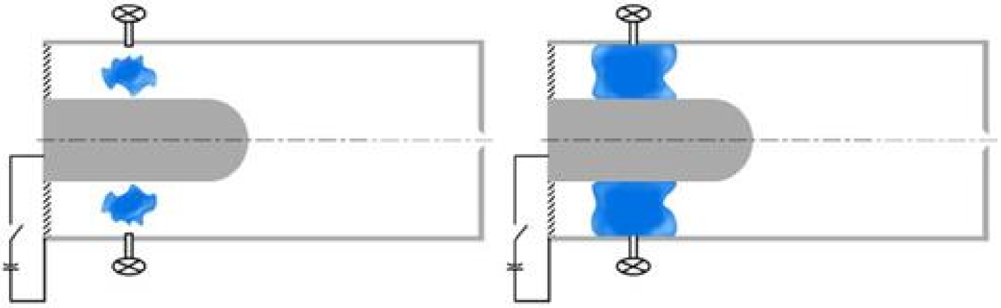

(a) Gas injection $t = t_1$ (b) Gas expansion $t = t_2$

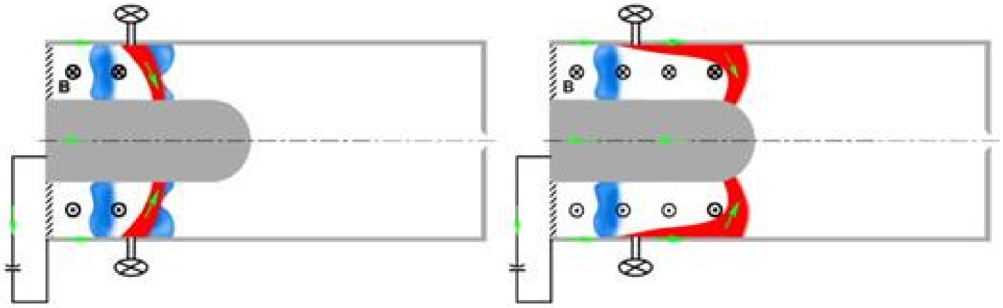

(c) Gas breakdown $t = t_3$ (d) Plasma acceleration $t = t_4$

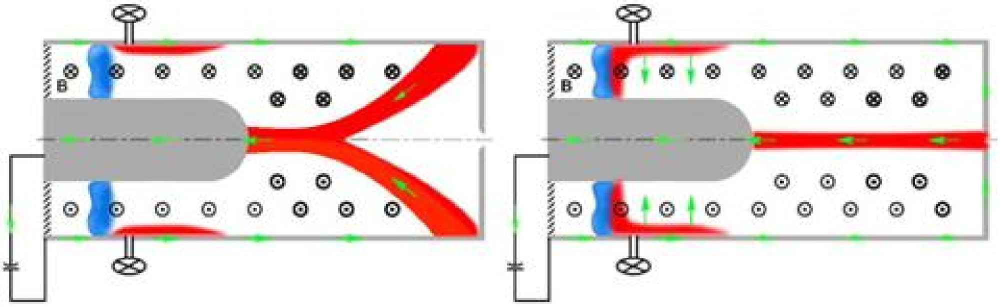

(e) Z-pinch formation $t = t_5$ (f) Z-pinch sustainment $t = t_6$

Figure 2.2: This image demonstrates a simplified version of the formation of the sheared-flow z-pinch plasma. Image (a) shows the initial introduction of hydrogen gas into the acceleration region of the axial chamber. After this, the gas begins to expand and fill the chamber as depicted in image (b). The capacitors are then charged and engaged, establishing a high potential across the electrodes that ionizes the gas between them (c). The plasma will then generate its own magnetic field as the electric field creates a current facing towards the inner electrode, causing the Lorentz force to push it down the length of the chamber (d). Once the acceleration terminus is reached, the plasma detaches and begins re-combining in a "zipper" fashion in the assembly region (e). A z-pinch is then formed with the sheared flow plasma along the length of the assembly region (f). [4]

on component sizes, Figure 2.1 provides this information.

Plasma Current (kA)	300
Pinch Current (kA)	150
Pinch Radius (cm)	0.3
Electron Density (m^{-3})	$10^{22} - 10^{23}$
Electron Temperature (keV)	1
Peak Total Mass Density (kg/m^3)	1.67×10^{-4}
Peak Total Pressure (MPa)	32

Table 2.1: ZaP-HD plasma parameters

2.2 Magnetic Field Diagnostic Setup and Data Collection

The magnetic field data used in the analysis of ZaP-HD's wave spectrum is recorded using field probes positioned within the assembly region depicted in Figure 2.1. As previously stated, they are positioned 5 cm apart from each other from the beginning of the assembly region to the end wall. At every 15 cm interval, the probes are laid out in an azimuthal array of 8. Every other probe position 5 cm apart has 4 probes. These are marked internally using the letter P with the number of centimeters they are into the assembly region chamber starting from the nosecone and ending at the endwall of the device. For example, P25 would mean 25 cm into the chamber and P30 would mean 30 cm into the chamber. These values will be used for the sake of succinctness. This totals to 56 probes within the entirety of the assembly region. On a brief note, there are also 15 field probes in the acceleration region but since the research in this paper is limited to the "quiescent" period of operation with highest stability, the transient acceleration period is not being considered [19]. Structurally, the probes consist of 32-gauge wire wrapped around a Kel-F form. This form is connected to a boron nitride shield with Torr-Seal, allowing for better protection against contact with the plasma [17]. These probes are inserted into machined holes in the electrodes at the wall of the assembly region and secured with silver-plated screws [22]. The data pulled from the probes is then digitized at a 40 MHz rate through Joerger TR1612 12-bit digitizers [17]. The digitized data is then accessed through readout programs like jscope or MATLAB plugins of MDSPlus as depicted in Figures 2.3, 2.4, and 2.5. In terms of time resolution of the probes, there is gap of 25 ns between each output value. This creates a maximum limit on the frequency of waves that can be studied.

2.3 Magnetic Field Probe Theory and ZaP-HD Stability

Due to the fact that the magnetic field in ZaP-HD is time varying, a voltage is produced across the field probes following Faraday's Law where $V = -\frac{d\phi}{dt} = -NA\frac{dB}{dt}$. To calculate the axial current and current centroid from the raw azimuthal field data, a Fourier decomposition of the form

$$B_\theta(\theta_i) = \sum_{j=0,m} a_j \cos(j\theta_i) + \sum_{j=1,m} b_j \sin(j\theta_i) \tag{2.2}$$

where θ_i is the azimuthal location of the prob[19][20][22]. In order to find the Fourier mode amplitudes for each sinusoidal contribution, the coefficients a_j and b_j in the series can be used in the equations

$$m_j = \sqrt{{a_j}^2 + {b_j}^2} \tag{2.3}$$

$$\phi_j = \tan^{-1}\left(\frac{b_j}{a_j}\right) \tag{2.4}$$

after using a matrix inverse to extract the coefficients [19][20][22]. In order to fully resolve the mode m_j, a probe array of $2m_j + 1$ is required. The $m = 1$ "kink" mode and the $m = 0$ "sausage" mode are, as stated earlier, respectively related to to the linearity/radial displacement from the geometric center of the pinch and the mean amplitude of the magnetic field. The $m = 1$ mode is also useful for its ability to predict the quiescent period of highest stability. The ratio of these two modes can relate to the radial current displacement as shown by

$$\frac{m_1}{m_0} = 2\frac{\Delta r}{r_{wall}} \tag{2.5}$$

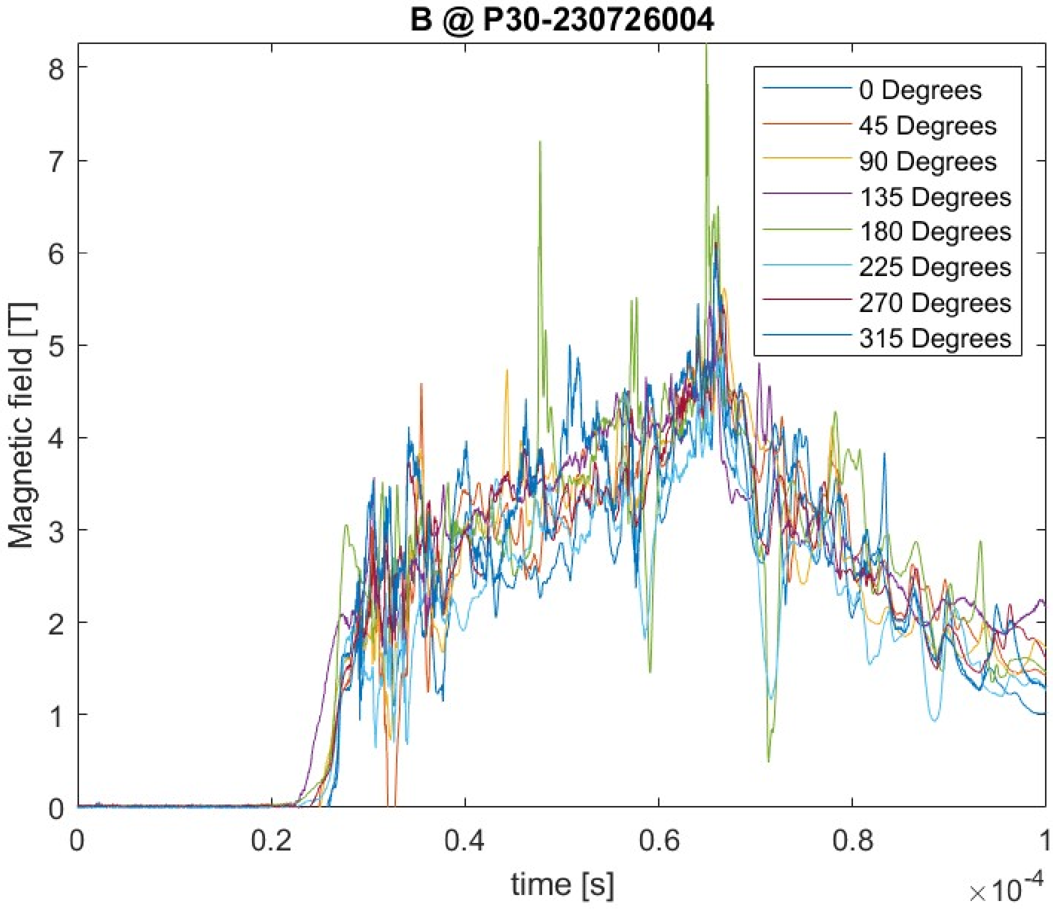

Figure 2.3: Digitized magnetic field readings from the P_{30} probe array. Note the 8 azimuthal readings at 45 degrees equally spaced from each other. As stated earlier, there are 4 positions at 15 cm intervals where the 8-probe array is utilized. Due to the higher amount of azimuthal probes affording a higher number of data points, these locations were chosen for the analysis for radial-propagating wave behavior.

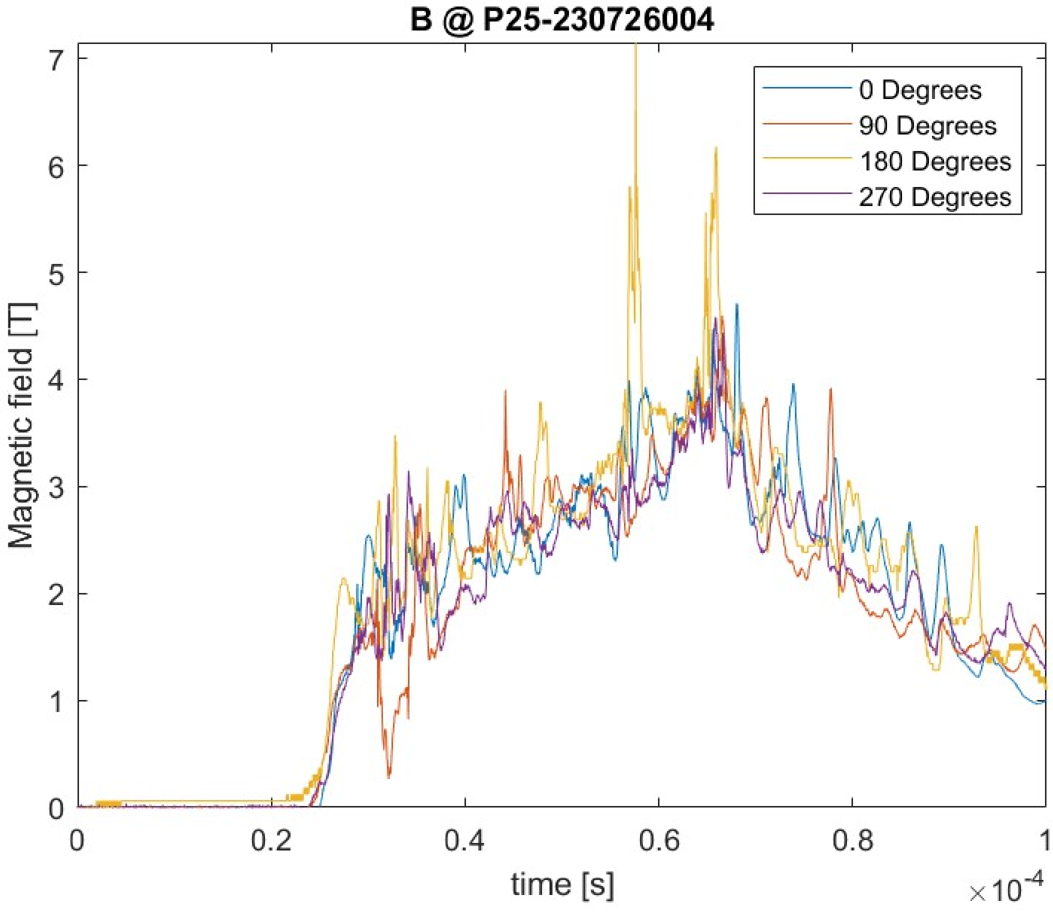

Figure 2.4: Digitized magnetic field readings from the P_{25} probe array. Note the 4 azimuthal readings at 90 degrees equally spaced from each other. Every remaining probe array not at the 15 cm intervals contain this 4-probe array. This difference between the probe counts contributes to a limit on the analysis for axial-propagating wave behavior that will be discussed in more detail later.

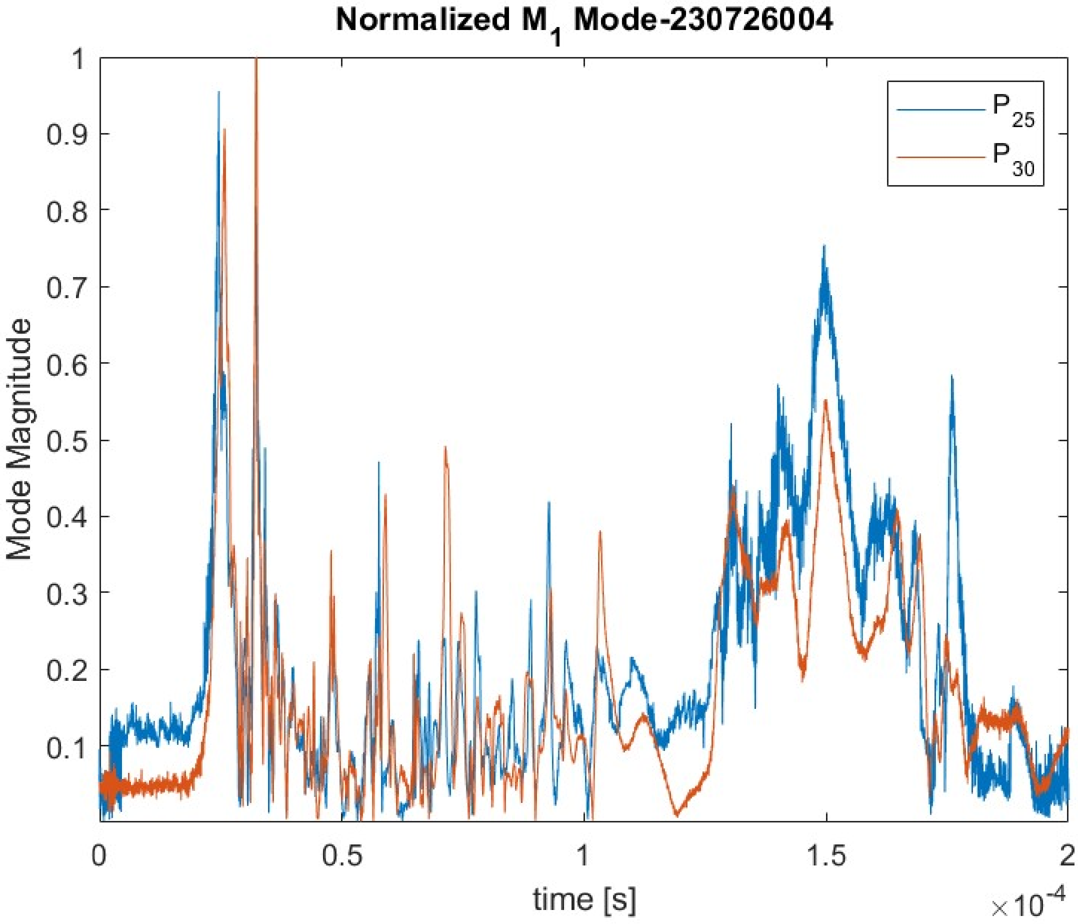

Figure 2.5: Illustration of the normalized $m = 1$ mode for positions P_{25} and P_{30} within the assembly region. This gives an idea of the length of time known as the "quiescent" period lasting from around 40 μs to 80 μs where there is low incidence of the MHD modes that lead to z-pinch failure. Once this period passes around 100 μs, however, these modes start to reappear and cause the stability of the pinch to fail and the pulse to end.

with the assumption that uniform axial current perturbations are present and the ratio $\frac{\Delta r}{r_{wall}}$ equates to less than 0.5 [22]. If the mode ratio is less than 0.2 and $m_0 > 0$ for an extended period of time, ZaP-HD is considered to be in a stable regime [17][23]. This stability can be seen in Figures 2.3 and 2.4 where the $m = 1$ mode hits a minimum during the quiescent period between roughly 40 and 80 microseconds. This corresponds to the peak in both current and magnetic field recorded by the probes. In Figure 2.5, the ratio of the two modes is graphed to visually illustrate the relationship between the stability of the pinch and the radial displacement away from the central axis.

2.4 ZaP-HD Applications

There are many applications that ZaP-HD could be successfully adapted for due to its unique sheared flow design beyond being just a z-pinch. With its simplistic geometry and hardware from lack of components like external coils, it can outpace other classical z-pinch concepts in stability performance for the push to a net positive reactor [13]. If the fusion reactor concept is unsuccessful, however, there is a potential use for acting as a neutron source that applies to a wide variety of situations [24]. Another potential future use for this design is as a spacecraft thruster. Nuclear fusion thrusters have been shown to be highly efficient and energy-intensive propulsion systems that will be one of the most powerful tools for exploring the outer solar system and potentially near-interstellar space. With a specific impulse numbering in the potentially thousands of seconds while matching the thrust output capabilities of a chemical system, it shows great promise [25].

However, there are several important considerations when implementing a fusion system as a spacecraft thruster. A significant hurdle is the mass and volume limitations a spacecraft presents for any type of power plant or engine. Notably, fusion reactors are heavy and large objects and this scales with the higher power requirements for a system with higher specific impulse. This movement towards more powerful and heavier reactors can result from the need to overcome bremsstrahlung radiation losses at high plasma temperatures [25]. ZaP-HD

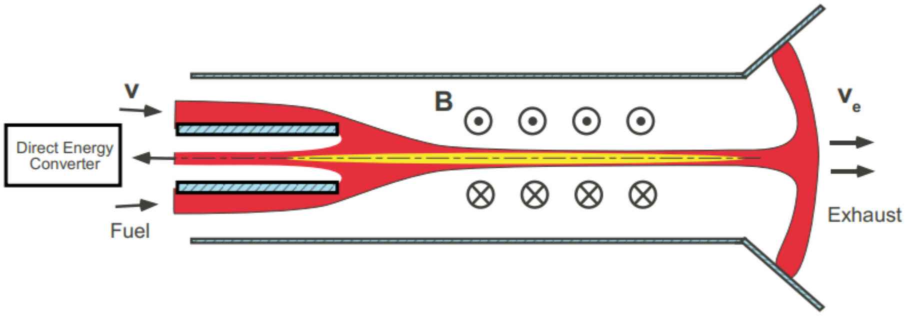

Figure 2.6: A simplified representation of how a specifically sheared-flow z-pinch fusion thruster would operate. Unlike the reactor design, however, it has a diffusing outer electrode for improved performance. A direct energy converter is also shown that greatly benefits the efficiency of the thruster. This direct energy converter modifies the closed nosecone design present within ZaP-HD currently. [5]

as a z-pinch might be able to mitigate some of these weight issues as a thruster the same way it does for terrestrial power: with the above mentioned benefits of compactness. Also, due to ZaP-HD's high plasma density (around 10^{23}m^{-3}), aneutronic fuel sources that reduce the need for additional neutron shielding can be utilized more easily [5]. This is on top of the benefits aneutronic fuel provides for direct energy conversion and thrust (discussed shortly).

There are several ways a device like this can be used within a spacecraft: the thermal method which requires many extra components for energy conversion and is limited by thermodynamic efficiency, the electric propulsion power plant method which has similar issues but for conversion to electrical power, and the method of direct energy conversion. Unlike the other two methods, DEC takes the reactor charged product particles and electronically redirects them for power while leaving the rest to be magnetically directed into forward thrust using components like a magnetic nozzle. It is both energy efficient and heavily reduces the requirement for hefty components like radiators, working fluids, turbines, and generators [26]. By its nature DEC also encourages aneutronic fuel to maximize charged products, which z-pinch's themselves also encourage. Together, z-pinches like ZaP-HD using DEC can combine their mass and volume-saving benefits to great effect to create a smaller and stronger thruster. Looking at the individual performance parameters of ZaP-HD as a thruster that can directly exhaust its fusion products compared to other traditional designs, the exhaust velocity reaches 100 km/s which equates to a specific impulse of about 10,000 seconds [27].

Chapter 3

PREDICTIVE MODEL FOR WAVEFORMS

3.1 Goals and Methodology

The purpose for this work is to establish a full predictive spectral model for the plasma waves both oscillatory and unstable with its inputs tailored to the parameters of ZaP-HD. Beyond that, it will be used as a tool to explore previously discussed wave phenomena like reactor heating for ZaP-HD. This represents a small section of that work by focusing on the MHD sub-region oscillatory modes in a cylindrical geometry. As will be shown, there is plenty of information that can be gathered from just analyzing the MHD spectrum. The predictive analysis will be inputted with observed data like the magnetic field, density, pressure, and flow velocity in radially defined mathematical profiles and compared with frequency analysis work later on to either corroborate the initial model or illuminate issues that can be resolved with modifications. This whole process is iterative and the research presented is the first few iterations towards the full model.

3.2 MHD Plasma Wave Basics

Before getting into the analysis of plasma waves, it would be best to describe the MHD regime itself. MHD models describe a single fluid model of a plasma containing both ions and electrons. As shown below in its ideal form

$$\rho\left(\frac{\partial \mathbf{v}}{\partial t}+\mathbf{v}\cdot\nabla\mathbf{v}\right)=-\nabla p+\mathbf{j}\times\mathbf{B} \tag{3.1}$$

$$\mathbf{j}=\nabla\times\mathbf{B} \tag{3.2}$$

$$\frac{\partial p}{\partial t}=-\mathbf{v}\cdot\nabla p-\gamma p\nabla\cdot\mathbf{v} \tag{3.3}$$

$$\frac{\partial \mathbf{B}}{\partial t} = \nabla \times (\mathbf{v} \times \mathbf{B}) \tag{3.4}$$

$$\nabla \cdot \mathbf{B} = 0 \tag{3.5}$$

$$\frac{\partial \rho}{\partial t} = -\nabla \cdot (\rho \mathbf{v}) \tag{3.6}$$

where $\mathbf{v}$ is the velocity field, $\mathbf{B}$ the magnetic field, ρ the single fluid density, and p the single fluid pressure, the MHD equation set combines inertial fluid mechanics with Maxwell's equations to generate a full model. When it comes to how to separate MHD phenomena from others within the plasma, it can be simply described by the following:

$$\lambda_{MHD} \approx a >> R_i \tag{3.7}$$

$$\tau_{MHD} \approx a/v_a >> \Omega_i^{-1} \tag{3.8}$$

where v_a is the Alfvén speed, R_i is the cyclotron radius, Ω_i is the cyclotron frequency, and a is the plasma radius. This contextualizes the model as depicting processes of low frequency, large size, and lower energy. Considering only MHD waves, as a result, removes the necessity of understanding statistical particle behavior or high temperature effects.

When analyzing the waveforms present in a plasma, it is best to start with a linear perturbation analysis of the various particle vector fields. To begin with, a static non-flowing plasma will be the basis for the model but this is corrected later. This can be shown with an additive perturbed vector field on top of the zero order stable state

$$\mathbf{v}(\vec{r}, t) = \mathbf{v}_1(\vec{r}, t) \tag{3.9}$$

$$p(\vec{r}, t) = p_0(\vec{r}) + p_1(\vec{r}, t) \tag{3.10}$$

$$\mathbf{B}(\vec{r}, t) = \mathbf{B}_0(\vec{r}) + \mathbf{B}_1 \vec{r}, t) \tag{3.11}$$

$$\rho(\vec{r}, t) = \rho_0(\vec{r}) + \rho_1(\vec{r}, t) \tag{3.12}$$

where f_0 represents the stable state of the particle system and f_1 represents a linear perturbation on top of this state usually taking the form of a Fourier mode. The Fourier mode, as shown by

$$A_1 = A_0 \text{exp}(i(\vec{k} \cdot \vec{r} + m\theta - \omega t)) \tag{3.13}$$

where k is the spatial wavenumber inversely associated with wavelength, m is the azimuthal mode number, and ω represents angular frequency related to frequency by a factor of 2π. From the k and ω quantities you can calculate two basic waveform properties known as the phase and group velocities. These two quantities, shown respectively as $v_p = \frac{\omega}{k}$ and $v_g = \frac{\partial\omega}{\partial k}$ where phase velocity represents the velocity of a wave phase and the group velocity represents the velocity of wave packets. Group velocity signifies the direction and amplitude of wave energy propagation. Another useful metric of depicting these quantities and wave properties in general is known as the index of refraction. This quantity, known for its inclusion in Snell's Law and signified by the letter n, can help shorten the various wave dispersion relations for a plasma. As a measurement metric, it can help describe wave speed in comparison to the speed of light. For example, if the index is larger than 1, the phase speed of a wave is slower than the speed of light while an index less than 1 would mean the opposite. With the fundamental assumption of low-amplitude and linear perturbations on top of the static medium and fields, it is possible to linearize the MHD equations as follows

$$\rho_0 \frac{\partial \mathbf{v}_1}{\partial t} = -\nabla p_1 + \mathbf{j}_1 \times \mathbf{B}_0 + \mathbf{j}_0 \times \mathbf{B}_1 \tag{3.14}$$

$$\mathbf{j}_1 = \nabla \times \mathbf{B}_1 \tag{3.15}$$

$$\frac{\partial p_1}{\partial t} = -\mathbf{v}_1 \cdot \nabla p_0 - \gamma p_0 \nabla \cdot \mathbf{v}_1 \tag{3.16}$$

$$\frac{\partial \mathbf{B}_1}{\partial t} = \nabla \times (\mathbf{v}_1 \times \mathbf{B}_0) \tag{3.17}$$

$$\nabla \cdot \mathbf{B}_1 = 0 \tag{3.18}$$

$$\frac{\partial \rho_1}{\partial t} = -\nabla \cdot (\rho_0 \mathbf{v}_1) \tag{3.19}$$

In order to further simplify this model, a Lagrangian displacement vector field $\boldsymbol{\xi}$(r,t) of a plasma element away from the equilibrium state is used [8]. Lagrangian operators involve moving the reference frame to be in line with the fluid in motion and lead to the conversion of

$$\mathbf{v} = \frac{D\boldsymbol{\xi}}{Dt} = \frac{\partial \boldsymbol{\xi}}{\partial t} + \mathbf{v} \cdot \nabla \boldsymbol{\xi} \tag{3.20}$$

But due to linearization, this can be just reduced to $\mathbf{v} \approx \mathbf{v}_1 = \frac{\partial \boldsymbol{\xi}}{\partial t}$. This converts portions of the linearized MHD model into the following forms:

$$p_1 = -\boldsymbol{\xi} \cdot \nabla p_0 - \gamma p_0 \nabla \cdot \boldsymbol{\xi} \tag{3.21}$$

$$\mathbf{B}_1 = \nabla \times (\boldsymbol{\xi} \times \mathbf{B}_0) \tag{3.22}$$

$$\rho_1 = -\nabla \cdot (\rho_0 \boldsymbol{\xi}) \tag{3.23}$$

With these converted terms introduced into the linearized MHD model, the MHD equation of motion can be derived such that

$$\mathbf{F}(\boldsymbol{\xi}) = -\nabla \pi - \mathbf{B} \times (\nabla \times \mathbf{Q}) + (\nabla \times \mathbf{B}) \times \mathbf{Q} = \rho \frac{\partial^2 \boldsymbol{\xi}}{\partial t^2} \tag{3.24}$$

$$\pi = -\gamma p \nabla \cdot \boldsymbol{\xi} - \boldsymbol{\xi} \cdot \nabla p \tag{3.25}$$

$$\mathbf{Q} = \nabla \times (\boldsymbol{\xi} \times \mathbf{B}) \tag{3.26}$$

This equation of motion will be the starting point for the derivation MHD cylindrical wave equation also known as the Hain-Lüst equation [8].

3.3 Hain-Lüst Equation

In order to arrive at the final result, it would be best to start with the type of geometry being used for this scenario. Z-pinches, like ZaP-HD, are cylindrical plasmas that contain an azimuthal magnetic field. This predictive MHD model based on the Hain-Lüst equation includes magnetic field orientations other than azimuthal so is generally applicable to many types of field geometries [8]. As shown in Figure 3.1, the model revolves around this "diffuse" plasma geometry. On top of this, the model uses a 1D radial inhomogeneity where there is a profile of $\rho(r)$, B(r), and p(r) [8]. The exact form of these profiles will be discussed later. With the initial equation set up, it is important to include a vector basis within this radial geometry to build from. Three unit vectors containing magnetic field projections: $\mathbf{e}_r$, $\mathbf{e}_\perp = (0, B_z, -B_\theta)/B$, and $\mathbf{e}_\parallel = (0, B_\theta, B_z)/B$ can be introduced into the gradient operator

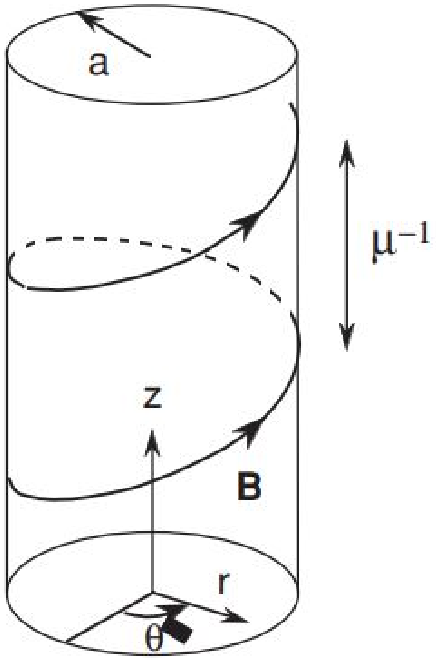

Figure 3.1: Depiction of a diffuse cylindrical plasma of radius a where both an azimuthal and radial component magnetic fields are present. However, for this analysis, the radial magnetic field component will be redundant to the final result. The symbol μ is representative of the ratio between the azimuthal and radial fields.

as a perturbed quantity such that $\nabla = \mathbf{e}_r \partial_r + i\mathbf{e}_\perp g + i\mathbf{e}_\parallel f$ [8]. The parallel and perpendicular operators now become algebraic multipliers of the form:

$$g = \frac{1}{B}(mB_z/r - kB_\theta) = \frac{G}{B} \tag{3.27}$$

$$f = \frac{1}{B}(mB_\theta/r + kB_z) = \frac{F}{B} \tag{3.28}$$

which can now be reintroduced into the vector basis and Lagrangian displacement field [8]. This creates three projections:

$$\xi = \mathbf{e}_r \cdot \boldsymbol{\xi} = \xi_r \tag{3.29}$$

$$\eta = i\mathbf{e}_\perp \cdot \boldsymbol{\xi} = i(B_z \xi_\theta - B_\theta \xi_z) \tag{3.30}$$

$$\zeta = i\mathbf{e}_\parallel \cdot \boldsymbol{\xi} = i(B_\theta \xi_\theta - B_z \xi_z) \tag{3.31}$$

which will be integrated into the original MHD equation of motion and then reduced to create the final Hain-Lüst radial geometry wave equation:

$$\frac{d}{dr}\left[\frac{N}{rD}\frac{d\chi}{dr}\right]\left[\frac{1}{r}H - \left(\frac{B_\theta^2}{r^2}\right) - \frac{4k^2B_\theta^2}{r^3 D}K + \left\{\frac{2kB_\theta G}{r^2 D}\left((\gamma p + B^2)H\right)\right\}'\right]\chi = 0. \tag{3.32}$$

$$K = B^2\rho\omega^2 - \gamma p F^2 \tag{3.33}$$

$$H = \rho\omega^2 - F^2 \tag{3.34}$$

$$N = (\rho\omega^2 - F^2)\left((\gamma p + B^2)\rho\omega^2 - F^2\right) \tag{3.35}$$

$$D = \rho^2\omega^4 - (m^2/r^2 + k^2)(\gamma p + B^2)\rho\omega^2 + (m^2/r^2 + k^2)\gamma p F^2 \tag{3.36}$$

This introduced a new variable ($\chi = r\xi$) that exists as a radial variable within the whole Hain-Lüst model. Now, this equation can be fully solved through either numerical or analytical methods through reduction to a first order PDE from its starting second order [8]. However, there is insightful information that can be gained by analyzing the singularities within the equation provided by the term $P = \frac{N}{rD}$. This will specify regions of continuous sub-spectra within the grand MHD discrete spectrum.

3.4 Singularities and Plasma Profile Assumptions

From the P term inside the generalized PDE, the N and D terms can take the form of

$$N(r;\omega^2) = \rho^2(\gamma p + B^2)[\omega^2 - \omega_A^2(r)][\omega^2 - \omega_S^2(r)] \tag{3.37}$$

$$D(r;\omega^2) = \rho^2[\omega^2 - \omega_{s0}^2(r)][\omega^2 - \omega_{f0}^2(r)] \tag{3.38}$$

where $\omega_A(r)^2$ is the Alfvén sub-spectra frequency, $\omega_S(r)^2$ represents the slow magnetosonic sub-spectra frequency, and $\omega_{s0}(r)^2/\omega_{f0}(r)^2$ represent something called a turning point frequency that represents a transitional frequency between the regions only containing sub-spectra frequencies. It will be discussed in more detail later [8]. A sub-spectra frequency represents regions within the entire MHD spectral regime dominated by and clustered around a certain type of propagating waveform (like the Alfvén wave for example) [8]. These four singularities can be separated out into their own forms such that:

$$\omega_A(r)^2 = F^2/\rho \tag{3.39}$$

$$\omega_S(r)^2 = \frac{\gamma p}{\gamma p + B^2} F^2/\rho \tag{3.40}$$

$$\omega_{s0,f0}(r)^2 = \frac{1}{2}(m^2/r^2 + k^2)\frac{\gamma p + B^2}{\rho}\left[1 + / - \sqrt{1 - \frac{4\gamma p F^2}{(m^2/r^2 + k^2)(\gamma p + B^2)^2}}\right] \tag{3.41}$$

These sub-spectra frequency singularities will be the beginning point from which the predictive model of ZaP-HD MHD phenomena will come from.

In order to complete this model setup, however, an approximation had to be made for both the magnetic field strength as well the plasma pressure and density. An extrapolation from the experimentally observed output is done to estimate magnitude at the plasma's surface and interior. To do this, Ampere's Law with an assumption of uniform current density and no current beyond the plasma radius is used giving the form $B_2/B_1 = r_1/r_2$ for the exterior working inwards from the wall and $B_2/B_1 = r_2/r_1$ for the interior of the plasma [21]. This will strengthen the field from the 10 cm wall to the 3 mm radius and weaken it as it passes into the plasma. For the density and pressure, a parabolic profile was utilized of forms

$$\rho = \rho_0 \left(1 - \frac{r^2}{a^2}\right) \tag{3.42}$$

$$p = p_0 \left(1 - \frac{r^2}{a^2}\right) \tag{3.43}$$

where 7 discrete radial locations were chosen (not including 0 and 3 mm) to measure the sub-spectra on as shown by Figures 3.2 and 3.3 [21]. The peak mass density and pressure are, as shown in Table 2.1, 1.67×10^{-4}kg/m^{-3} and 32 MPa respectively. The quadratic mathematical profile takes these peak values and decreases them to 0 at the surface edge of the plasma. The peak pressure was calculated by the state equation $P = nk_bT$. This analysis will also be performed along the 8 azimuthal probe locations.

3.5 Doppler Shift Correction

The basis of the model used in this research begins with the assumption of a static plasma within the z-pinch and with motion only in the linear perturbations applied to the equilibrium state. Within the context of ZaP-HD, this assumption cannot be used as there is a velocity profile present by its nature as a sheared-flow z-pinch. What this results in is a Doppler shift modification to all possible magnetic field signals that follow the form $\omega_f = \omega_0 + / - kv_d$ where ω_0 is the base frequency calculated from the ideal plasma Hain-Lüst derivation, k is the Doppler shift wavenumber, v_d is the velocity of the moving plasma, and ω_f is the final modified frequency of the wave [3]. In this research, an assumption was made that the plasma would always be traveling away from the probes towards the end wall and would thus cause the Doppler shift to elongate wave signals and decrease the final frequency. On top of this, the velocity of the flowing plasma was not assumed to be spatially uniform. It is known that the top speed of the plasma is about 100 km/s at its surface but this decreases to 0 km/s at the center where the static plasma model holds [28]. In order to achieve this gradient, a linear profile starting from 0 km/s at the 7 discrete radial locations is subtracted from the static frequency at said radius until 100 km/s is achieved on the surface of the

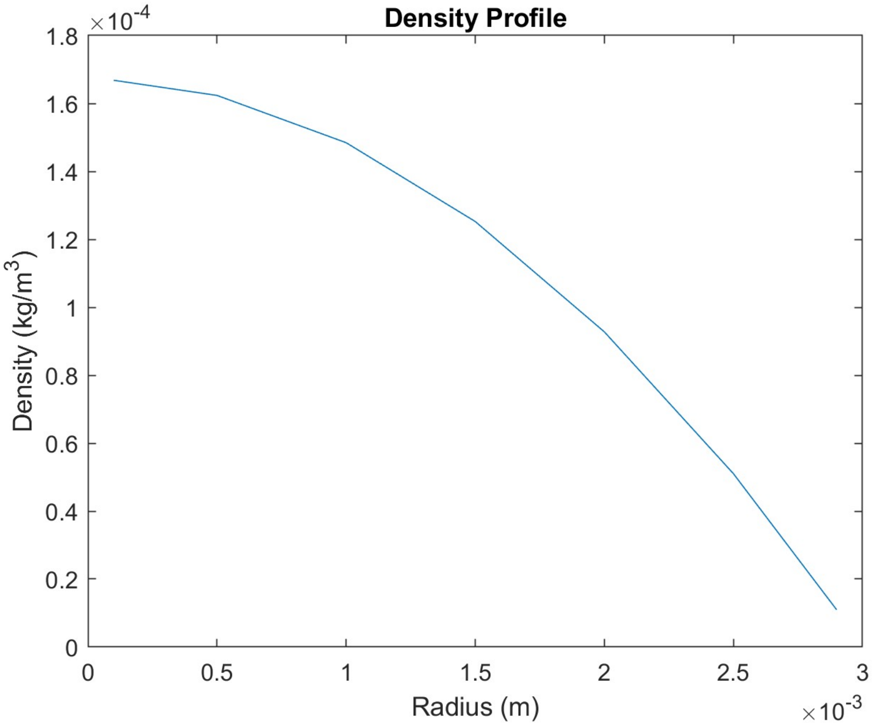

Figure 3.2: Illustration of the parabolic density profile with the 7 discrete radial locations of 0.1 mm, 0.5 mm, 1 mm, 1.5 mm, 2.0 mm, 2.5 mm, and 2.9 mm. The mass density begins at its peak of $1.67 \times 10^{-4}\text{kg/m}^{-3}$ at the center of the plasma and tapers off to 0 at the edge. 0 mm and 3 mm away from the plasma center were not chosen to avoid singularities in the model.

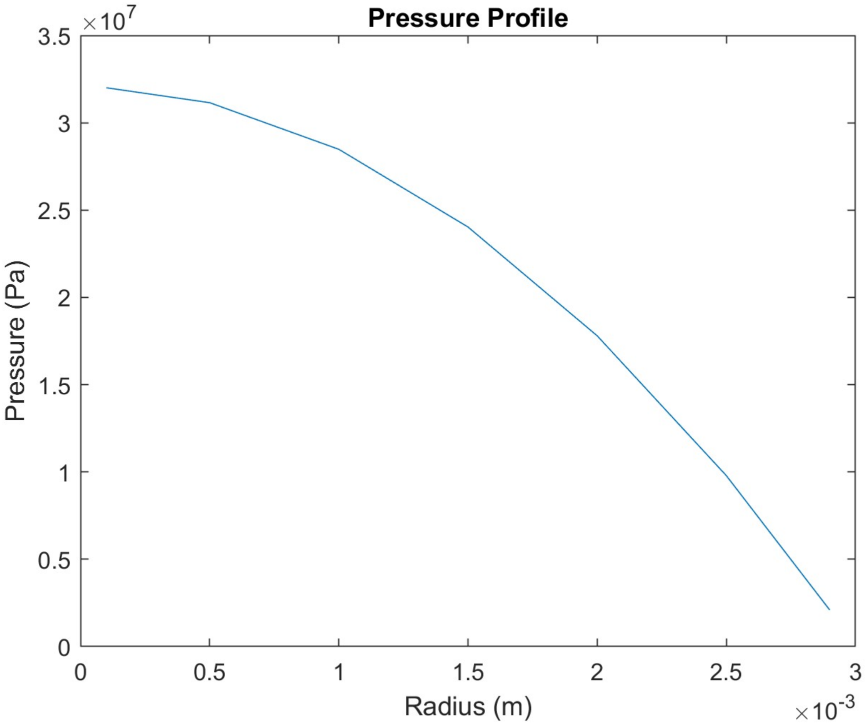

Figure 3.3: Illustration of the parabolic pressure profile with an identical appearance to the density profile and at the same 7 radial locations. Again, 0 mm and 3 mm away from the center are avoided to stop singularities from appearing. Peak pressure was related to density by the state function $P = nk_bT$.

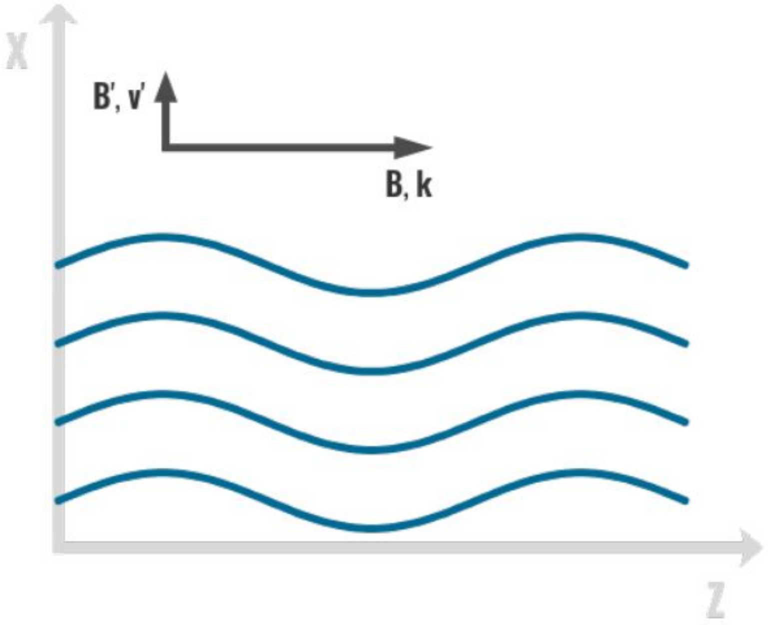

Figure 3.4: A visual for helping show the direction of travel of Alfvén waves relative to other plasma parameters. These parameters are: the equilibrium magnetic field (B) which is parallel to propagation, the perturbed magnetic field (B') which is perpendicular to propagation, and the perturbed velocity (v') which is perpendicular to propagation. [6][7]

plasma.

3.6 Alfvén Wave Behavior and Predicted Results

Alfvén waves are a type of MHD wave that is incompressible and propagates along the magnetic field lines. The linear perturbations assumed to generate the Alfvén run perpendicular to the direction of travel of the wave. In the context of a z-pinch, an Alfvén should travel azimuthally alongside the direction of the magnetic field. Figure 3.4 gives a useful graphic that helps visualize this process. With context established, the predictive model that starts with the Hain-Lüst Alfvén singularity is inputted with the profiles utilizing the previously discussed experimentally observed data like the magnetic field to yield the results shown in Figure 3.5. These same inputs will be used for the magnetosonic singularity and turning point frequency singularities. The focus for all studied wave phenomena is centered around the assembly region probe P30 for its higher radial probe count and to avoid issues with redundant results and mismatched digitized output array sizes making some frequency analysis methods impossible. As shown in the figure, the Alfvén sub-spectra frequency is between 10^7 and 10^8 rad/s. As the radius increases from the center of the plasma to the edge, the frequency jumps significantly.

3.7 Magnetosonic Wave Behavior and Predicted Results

In contrast to Alfvén waves, magnetosonic waves are compressible and propagate across magnetic field lines. This makes them run perpendicular to the equilibrium magnetic field vector alongside the perturbed magnetic field and velocity. Within the context of a 3-D environment like a z-pinch, this can include both axial or radial propagation. However, due to the absence of probes at multiple radii for the comparative frequency analysis, axial propagation will be considered only. Figure 3.6 should help visualize the motion of a magnetosonic wave. There is also a distinction between the fast and slow magnetosonic waves. Both have different propagation patterns and different frequency ranges. However, in the context of the Hain-Lüst model, the fast magnetosonic sub-spectra exists at infinity and therefore does not meaningfully apply for this research. Therefore, the analysis was conducted on the slow magnetosonic sub-spectra producing the results shown in Figure 3.7. Compared to the predicted frequency results given by the Alfvén sub-spectra, the magnetosonic frequencies appear within roughly the same range of 10^7 and 10^8 rad/s though in general less than the Alfvén frequencies at the same radial location. This validates the prediction of slow magnetosonic frequencies as they are generally lower than Alfvén waves as depicted in Figure 3.8 [8].

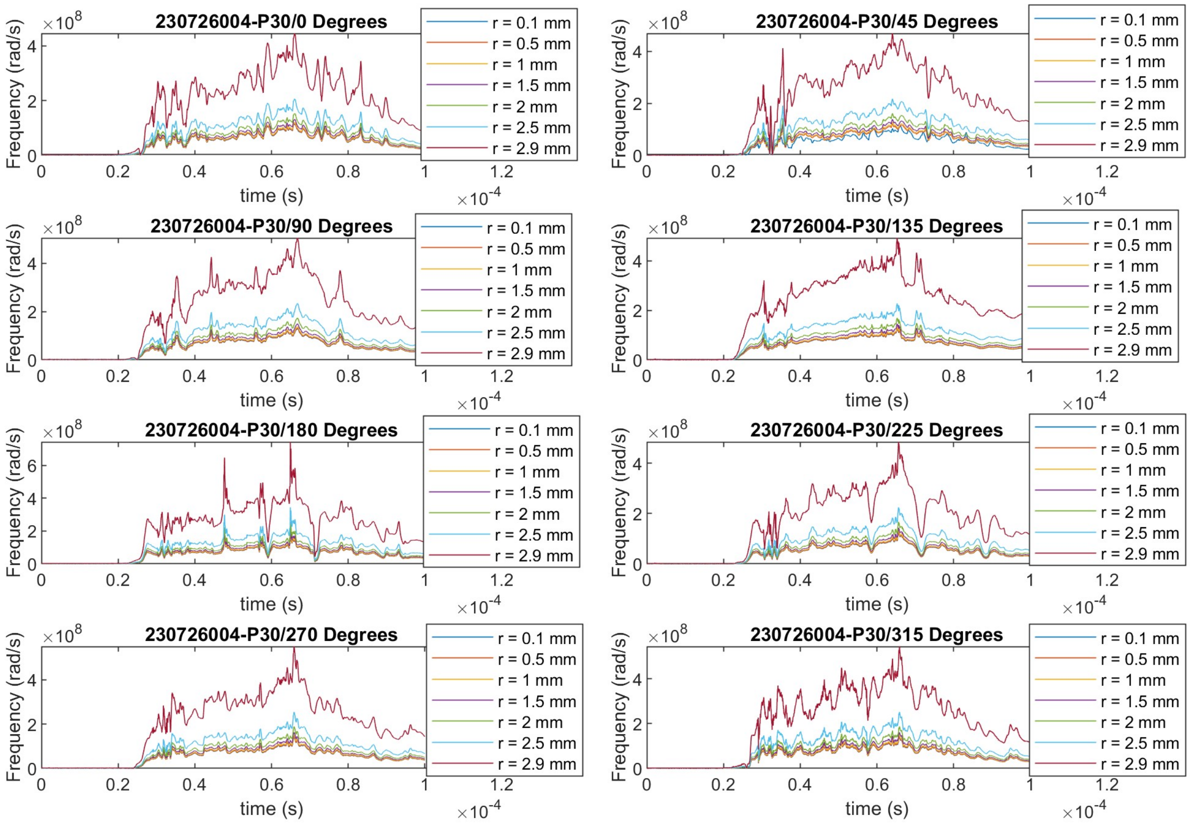

Figure 3.5: This predicted behavior of the Alfvén sub-spectra ($\omega_A(r)^2$) yields the following results for the 8 azimuthal locations within ZaP-HD at the 7 discrete radial locations mentioned earlier. It shows a strong correlation between frequency and radius owing to the strengthening magnetic field and shrinking density at higher radii shown an Eq. 3.37.

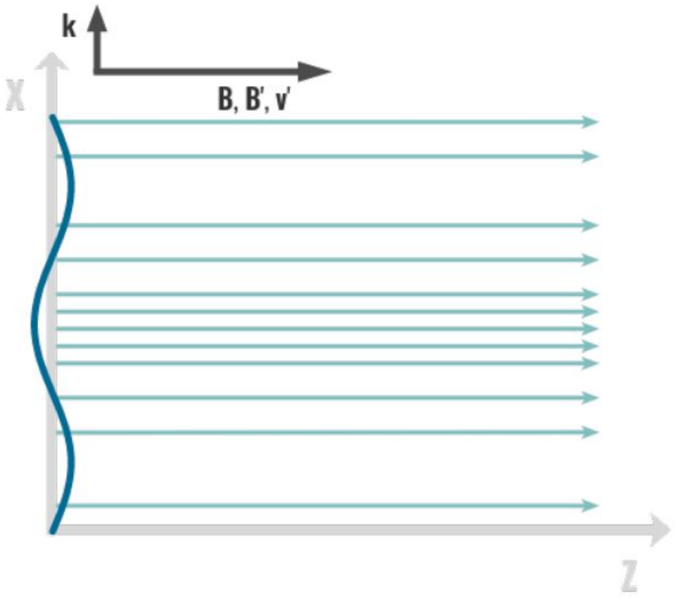

Figure 3.6: This visualizes the perpendicular propagation of a magnetosonic wave relative to other plasma parameters. Compared to Alfvén wave propagation, the equilibrium magnetic field (B) is now shown perpendicular to magnetosonic propagation. [6][7]

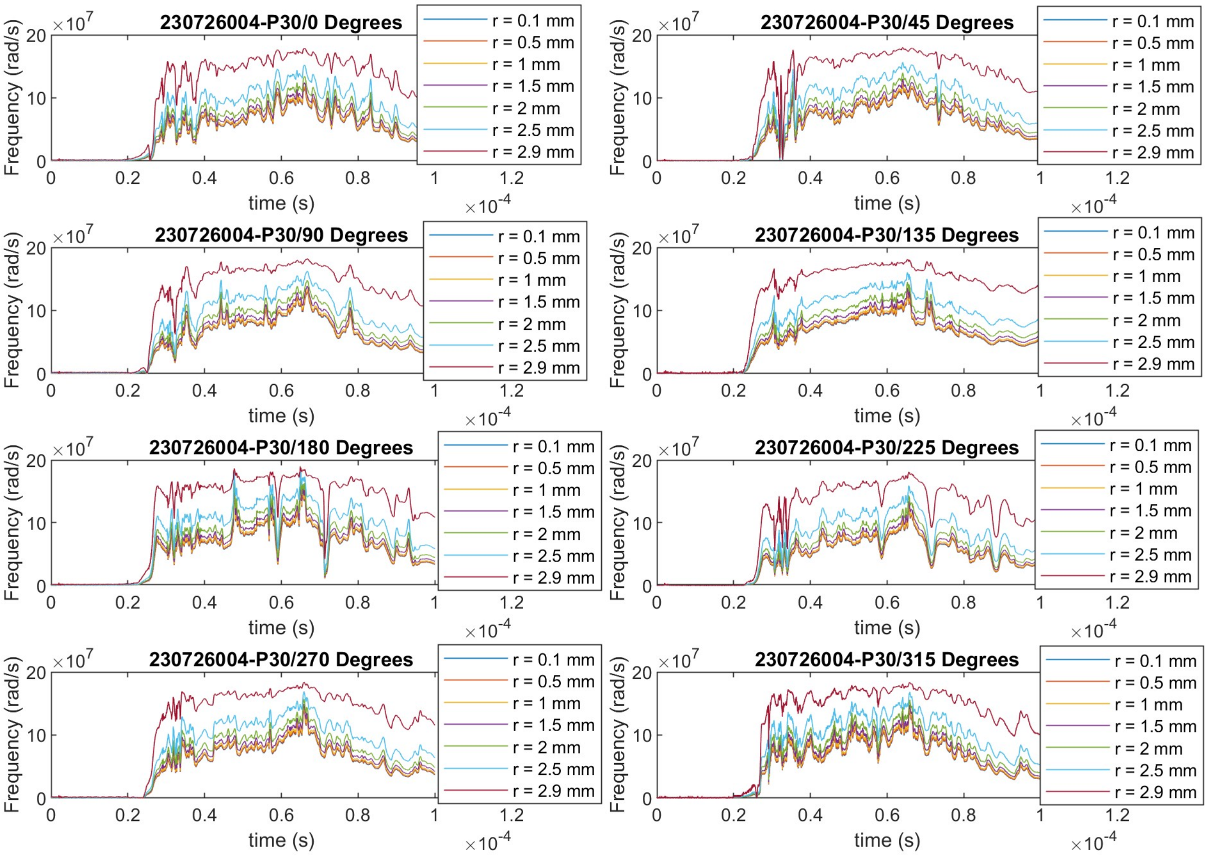

Figure 3.7: Results the following results of the slow mangetosonic sub-spectra ($\omega_S(r)^2$) for the 8 azimuthal locations within ZaP-HD at the 7 discrete radial locations mentioned earlier. As mentioned previously, the frequency range is less than but close to the Alfvén range which is expected. However, the radial correlation between radius and frequency is not as strong for slow magnetosonic waves due to its more complex dependence on the magnetic field and density/pressure profiles.

3.8 Turning Point Frequencies

Although the Hain-Lüst model has two “true” singularities that represent the continuous sub-spectra of the Alfvén and slow magnetosonic frequency regimes. Beyond these cluster points exists two “apparent” frequencies known as turning point frequencies [8]. In comparison to the Alfvén and magnetosonic regimes, these turning point frequencies do not dominate their own continuous region of the MHD spectrum like true sub-spectra (or “true” singularities) but act more as discrete gateways between each regime (hence the name) [8]. They also exist as a transition between wave propagation and evanescence (non-propagating oscillation) [8]. Once each turning point frequency is crossed, the frequency regimes start to gravitate towards the cluster points of the main continuous spectra like the slow or fast magnetosonic waves. As stated earlier, however, the fast magnetosonic regime doesn’t exist at a finite value in an inhomogeneous cylindrical plasma and is situated at infinity [8]. Nonetheless, the fast turning point frequency shows when this monotonic increase starts to take hold. A caveat exists, though, when having any kind of inhomogeneity in a cylindrical plasma. Overlap will start to occur the stronger the inhomogeneity becomes relative to other plasma processes and may cause wave interference that could lead to errors in predicted results [8]. Figure 3.8 can help with visualizing the ideal separation points amongst the full discrete spectrum into the sub-spectral regions. The turning points contain geometrical singularities and show a convergence to their continuous counterparts at the center of the plasma. For example, the slow turning point frequency behaves exactly like the slow continuous sub-spectra would at the center of the plasma while the fast turning point converges to infinity at the center in accordance with the fast sub-spectra. Figures 3.9 and 3.10 give the results of the model for the two turning point frequencies.

3.9 Prediction Model Analysis Summary

With the results outputted, there now exists an expected baseline from the assumptions established earlier going into the Hain-Lüst model and the profiles generated from the exper-

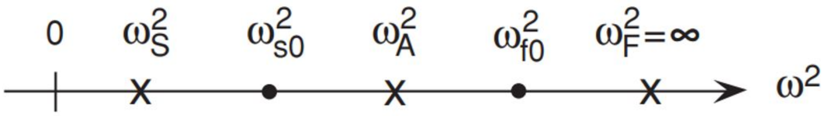

Figure 3.8: A visual for helping understand where the turning point frequencies are situated between the other other continuous essential sub-spectra. The slow turning point frequency exists between the domains of the slow magnetosonic and Alfvén sub-spectra. The fast turning point frequency does the same for the Alfvén and fast magnetosonic sub-spectra. However, as stated earlier, the fast magnetosonic domain is entirely at infinity within this model based on Hain-Lüst. [8]

imentally observed data like the magnetic field, velocity, density, and pressure. What this anticipates is that the whole spectral set exists between about 10^7 and 10^8 rad/s with Alfvén being higher than the slow magnetosonic region and the two turning points as midway between all the continuous areas. The model will now be compared with frequency analysis of ZaP-HD for possible future adjustment of said assumptions. There should be expectations about how the waves behave as they move within the z-pinch and how to read the probes. Alfvén waves should be detected by azimuthal probe locations due to it being parallel with the magnetic field and magnetosonic waves should be picked up by axial probe locations due to its behavior of propagating perpendicular to the magnetic field lines. Since magnetosonic waves move across field lines, it is possible in a three-dimensional space for there to be radial propagation. However, this can't be accounted for since only azimuthal and axial probes are present.

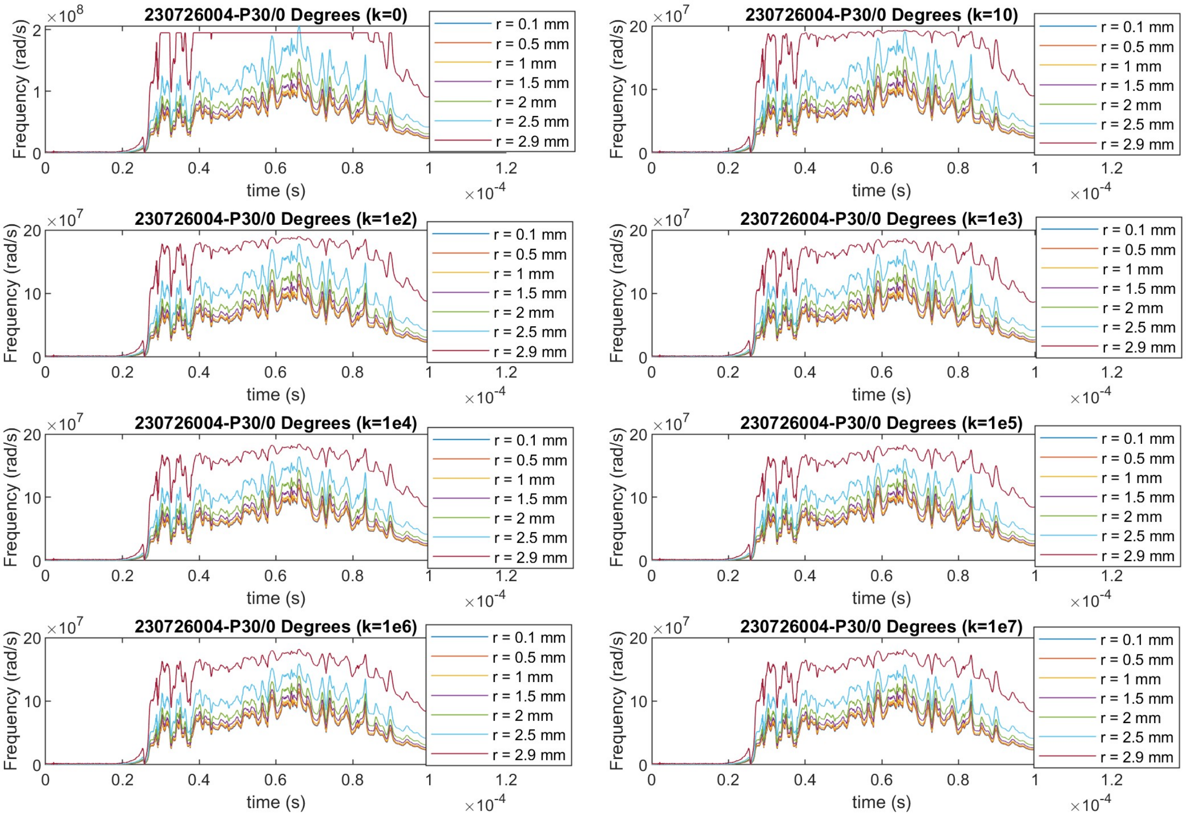

Figure 3.9: The results for the slow turning point frequency ($\omega_{s0}(r)^2$) illustrate how the frequency values look similar to the slow magnetosonic sub-spectra center-of-plasma behavior as it approaches r = 0 mm. There exists some saturation artifact at the 0 degrees location of unknown origin that does not appear in any of the other azimuthal readings.

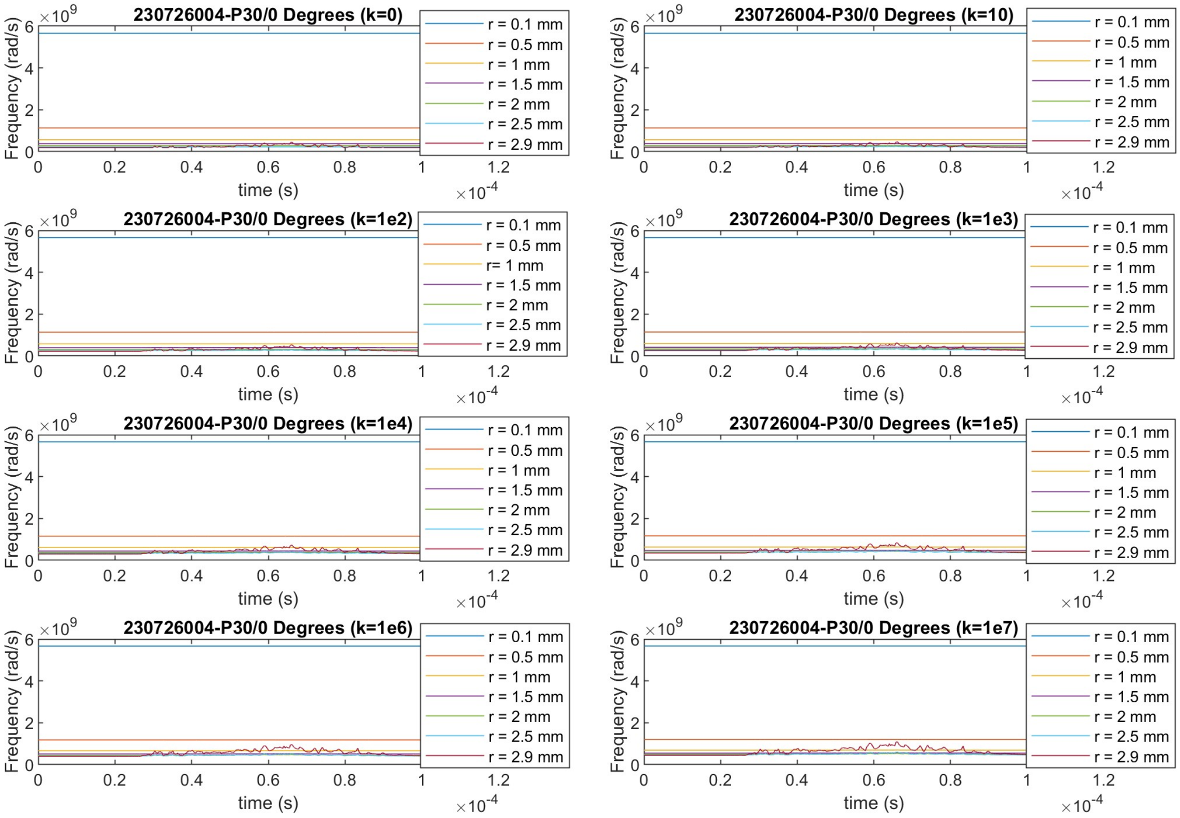

Figure 3.10: Contrasting with the slow turning point frequency, the fast turning point frequency ($\omega_{f0}(r)^2$) shows a quickly increasing asymptotic progression to infinity as it approaches lower radii with r = 0.1 mm being significantly higher than other locations further out. This matches it with the constantly infinity fast magnetosonic sub-spectra. The drastically different appearance between the slow and fast turning point frequencies can be explained by viewing Eq. 3.39 an seeing the plus or minus sign differentiating the two. Just changing the minus sign to a plus sign for the fast turning point frequency leads to this behavior.

Chapter 4

FREQUENCY ANALYSIS OF MAGNETIC FIELD PROBES

4.1 Motivation for Analysis and Correlation Basics

With the model giving a predicted behavior of the MHD spectrum, it needs to be checked with extracted frequencies from the magnetic field's periodic behavior. The model used the magnetic field data as well, but as a magnitude to be entered into the Hain-Lüst singularities. The basis of the frequency analysis will involve finding the periodicity within that data. Correlation, or for this research, cross-correlation is accomplished by the comparison of two arrays/sequences that are either deterministic or random. One signal is usually shifted with respect to the other to help find repeating behavior. In cases where the two arrays are fully random, the true cross-correlation sequence can be defined as

$$R_{xy}(m) = E\{x_{n+m}y_n^*\} = E\{x_n y_{n-m}^*\} \tag{4.1}$$

where n is from negative to positive infinity, the asterisk denotes complex conjugation, x and y are the stationary random sequences or arrays and E is the expected value [29][30]. However, the function used in MATLAB, *xcorr*, can only estimate the cross-correlation sequence, since only a finite segment of the infinite-length truly random processes are available. Raw correlations are calculated without normalization through

$$\hat{R}_{xy}(m) = \sum_{n=0}^{N-m-1} x_{n+m}y_n^*, \qquad m \geq 0 \tag{4.2}$$

$$\hat{R}_{xy}(m) = \hat{R}{}_{yx}^*(-m), \qquad m \leq 0 \tag{4.3}$$

A hat is used to indicate the estimate provided by the mathematical function *xcorr* in comparison to a fully randomized and infinite sequence. In most cases, the correlation function requires there to be a normalization process to produce an accurate estimate [29][30]. This can be accomplished by a biased estimate where

$$\hat{R}_{xy,\text{biased}}(m) = \frac{1}{N}\hat{R}_{xy}(m) \tag{4.4}$$

an unbiased estimate where

$$\hat{R}_{xy,\text{unbiased}}(m) = \frac{1}{N - |m|}\hat{R}_{xy}(m) \tag{4.5}$$

or normalized at zero where the correlation at zero lag between the two signals is equal to 1

$$\hat{R}_{xy,\text{coeff}}(m) = \frac{1}{\sqrt{\hat{R}_{xx}(0)\hat{R}_{yy}(0)}}\hat{R}_{xy}(m) \tag{4.6}$$

It is only possible to perform these normalizations if the sequence is of equal length, however. In that instance of unequal length sequences, a correlation without a normalization will suffice [30][29]. For this research, however, an unbiased normalization shown in Eq. 4.5 is performed.

4.2 Using Cross-Correlation Analysis with ZaP-HD Probe Limitations

This correlation analysis is demonstrated in Figure 4.1 where a test dataset is correlated with a delayed version of the same set. This was done to help aide in understanding the basic aspects of utilizing the method. Cross-correlation has many uses beyond those just discussed in this paper that rely on understanding trends and periodicity. For the context of this research, there are some caveats to where the cross-correlation analysis was performed. Due to the fact that the probes only output at a given radius (the wall), there is no radial distinction of the magnetic field and any previous extrapolations were magnitude estimations for the predictive model. This will mean only a single data point per angle was tested. As shown, the previous analysis and the frequency analysis after this are limited to the P25 and P30 locations within the assembly region. This is due to the fact that wave behavior over several axial locations proved redundant with similar results to the two chosen locations. Therefore, the findings of the research can be seen with just P25 and P30. Also, the magnetic field probes do not always output digitized data in equal array sizes. This becomes a problem specifically for axial probes motion and therefore only the 0 degrees location was able to be analyzed.

Before performing the cross-correlation, an initial correction had to be made to the magnetic field data from its raw form. Due to ZaP-HD having a rise and fall of its magnetic field during a pulse, this creates one easily detectable and low frequency period that needs to be removed to avoid the cross-correlation function tripping on it and producing a lowered extracted frequency. Figures 4.2 and 4.3 show the averaged results for both P25 and P30 that were subsequently subtracted from the raw output to leave only higher frequency behavior behind. With this averaging step completed, the correlation was performed between the azimuthal probes for the Alfvén waves and the axial probes for the magnetosonic waves. The *max* function was used to pull an index from the correlated data set and linked to a lag between the two original sets. This was then multiplied by the resolution rate of 25 ns to give the periodicity of an extracted signal.

4.3 Azimuthal Cross-Correlation Analysis Results and Prediction Comparison

With all the cross-correlation analysis completed on the azimuthal locations at P30, the output shown in Figure 4.4 gives a hint of what kind of periodic signal is getting picked up. The maximums found at each locations starting from 0 and ending at 315 degrees are as follows: 0 s (between 0 and 45 degrees), 0 s (45 and 90), 9.75×10^{-7} s (90 and 135), 3.58×10^{-5} s (135 and 180), 7.5×10^{-8} s (180 and 225), 7.5×10^{-8} s again (225 and 270), and 7.5×10^{-8} again (270 and 315). When put into the period/frequency relationship $\omega = \frac{2\pi}{T}$, this outputs frequency in rad/s. When comparing to the values given by the model of around 10^7 to 10^8 rad/s, the frequency analysis outputs around 10^6 to 10^7 rad/s for an Alfvén-like wave which lowers even more below 10^6 rad/s if the outlier frequencies are included. Possible model corrections for this discrepancy will be discussed later.

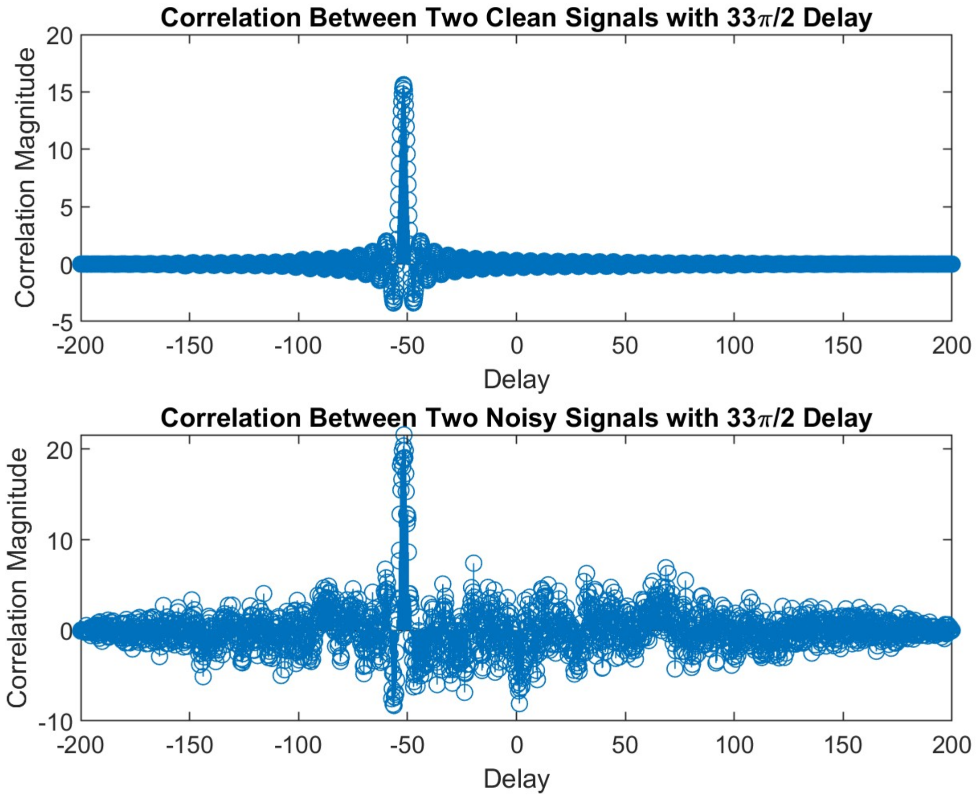

Figure 4.1: This is a test correlation analysis demonstrating the method. The top plot was acquired from delaying a non-noisy signal (sinc(x) function) with the same signal by a distance of $\frac{33\pi}{2}$ and correlating it with the original unaltered signal with a spike at 0. It is shown that the analysis has a correlation spike right at the delay amount. The lower plot was acquired from applying a random noise on top of the two clean superimposed sinc(x) signals to prove the cross-correlation function's effectiveness in noisier circumstances.

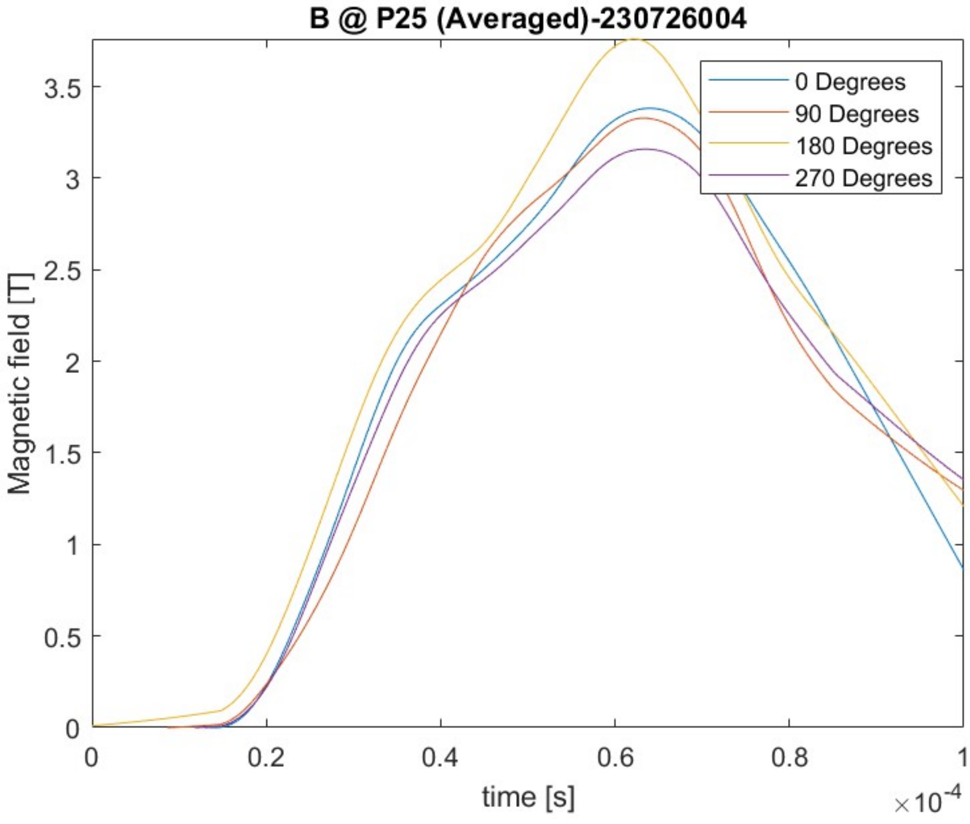

Figure 4.2: Shows the averaged data at P25 using the *smoothdata* function on the *lowess* setting. It is subsequently subtracted from the raw dataset. The function setting *lowess* creates a smoothed version of the raw data through a linear regression over the time window. This method creates less discontinuities than with a moving average. This probe average represents the low frequency behavior that the cross-correlation will detect and skew the results downward.

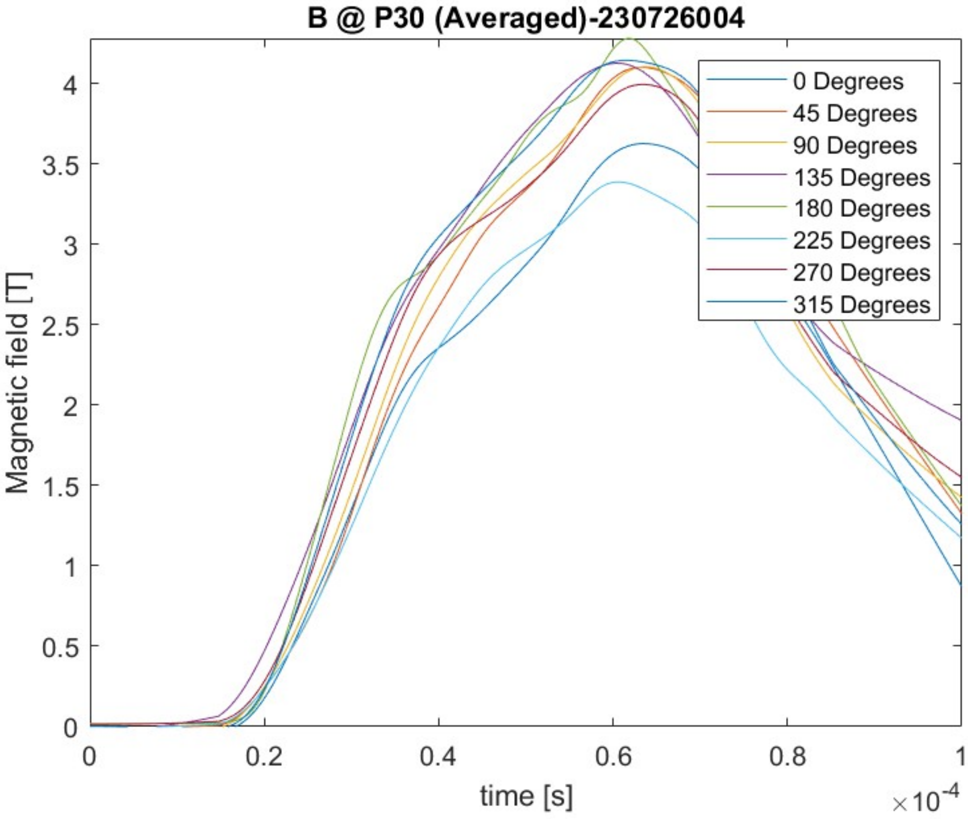

Figure 4.3: Shows the averaged data at P30 using the *smoothdata* function on the *lowess* setting. It is then subtracted from the raw output. This same method was done at this location to avoid discontinuities from a moving average smoothing method. This represents the same low frequency behavior but with an 8 azimuthal probe array.

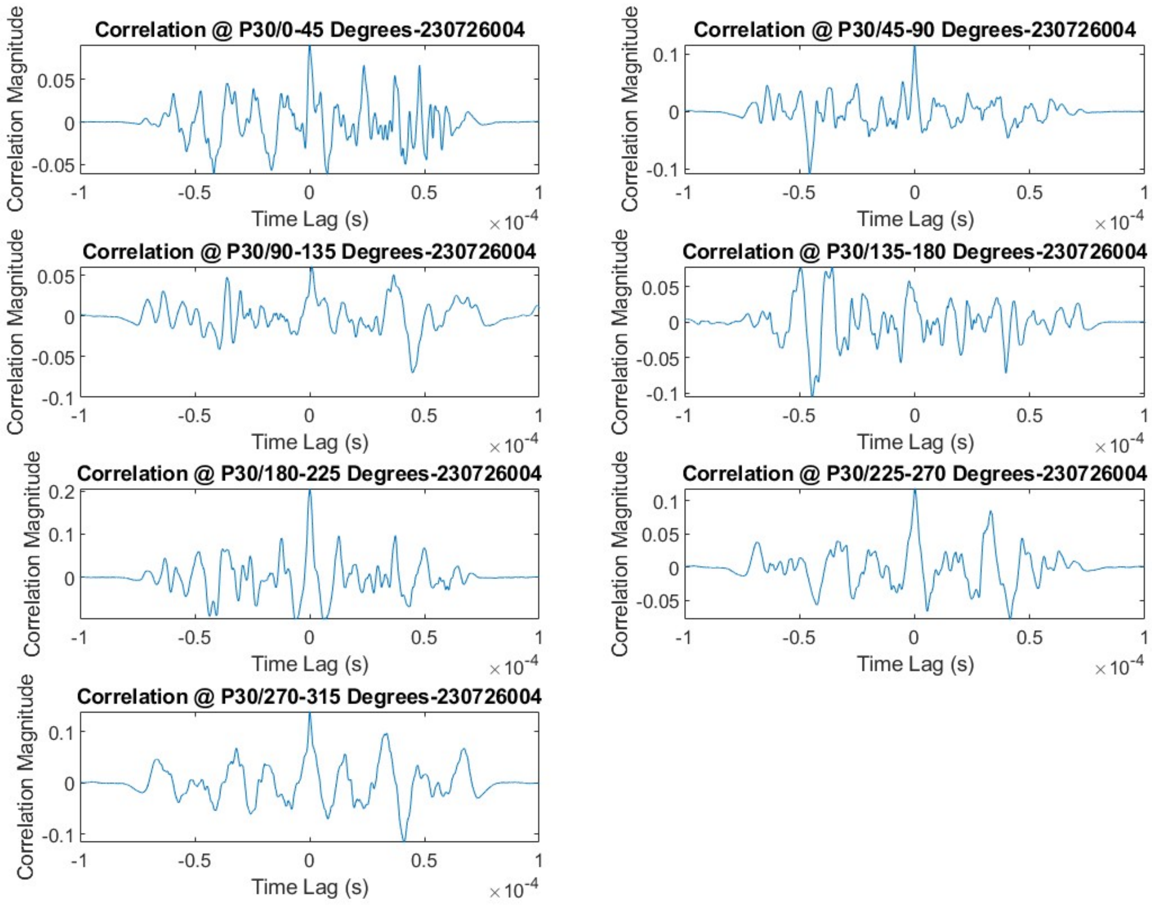

Figure 4.4: Illustrates the correlation between the magnetic field probes located at azimuthal positions in P30 are shown. The maximum in the graphs were found and the times (period) were inverted to find a frequency. Some of the cross-correlations (between 135 and 180 degrees) revealed maximums that were not close to zero that skewed the average. Despite that, the same takeaway still applies whether these are included or not in the average Alfvén frequency: there is a noticeable difference in predicted results from model and results taken from the frequency analysis.

4.4 Axial Cross-Correlation Analysis Results and Prediction Comparison

When analyzing the behavior from the axial probes, the earlier stated limitations apply and therefore only the zero degrees was looked at. This generates an cross-correlation analysis result as shown in Figure 4.5 with a similar issue present in the azimuthal result. The maximum found corresponds to a lag/period time of 2.75×10^{-7} s. This fits in that range of values somewhat separated from the predicted result like the aziumthal case and sits it around 10^6 rad/s for a magnetosonic-like wave. In order to corroborate this single data point on the axial analysis, a Fourier transform on the magnetic field data was done at P30/0 degrees and gives a result that seems in line with the Cross-correlation as shown in Figure 4.6. As mentioned previously in the Alfvén analysis, possible model corrections will be discussed to remedy this discrepancy found with the slow magnetosonic wave analysis.

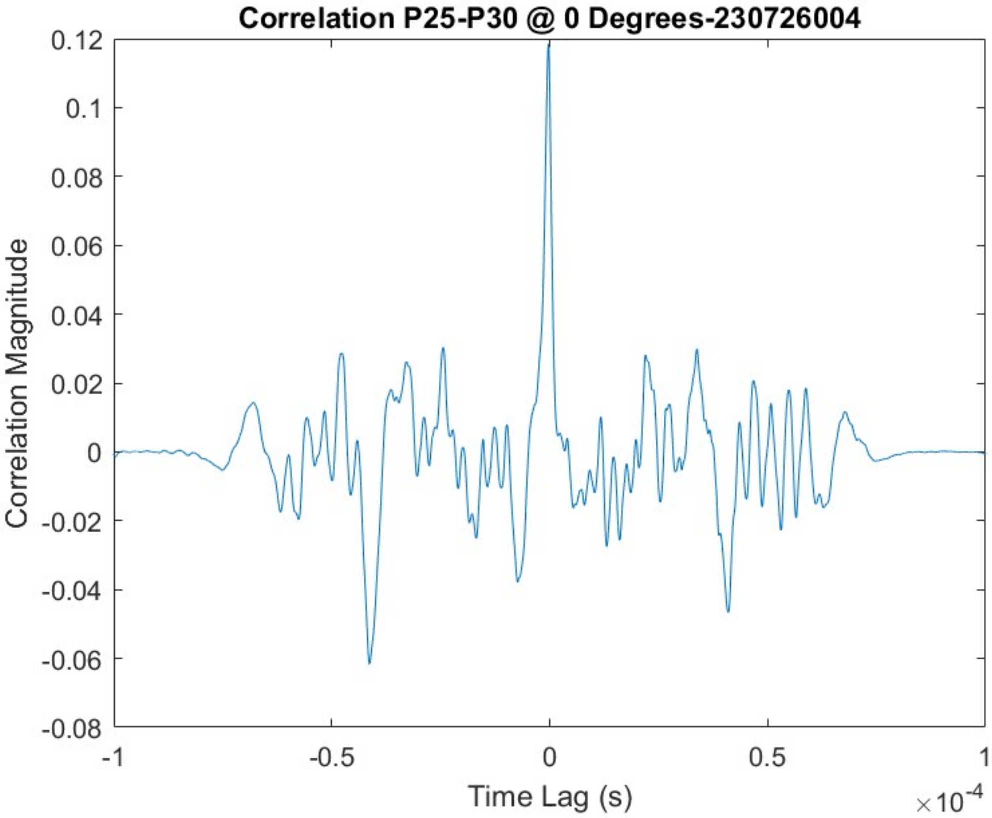

Figure 4.5: In this figure, the correlation between the magnetic field probes located at axial positions between P25 and P30 at zero degrees is shown. As in the Alfvén case, the maximum in the graph was found and the period was inverted to find a frequency. Despite the analysis being performed at only a single radial location, it shows a similar result from the Alfvén frequency results: that the axially propagating slow magnetosonic wave frequency does not match with that found in the predictive model.

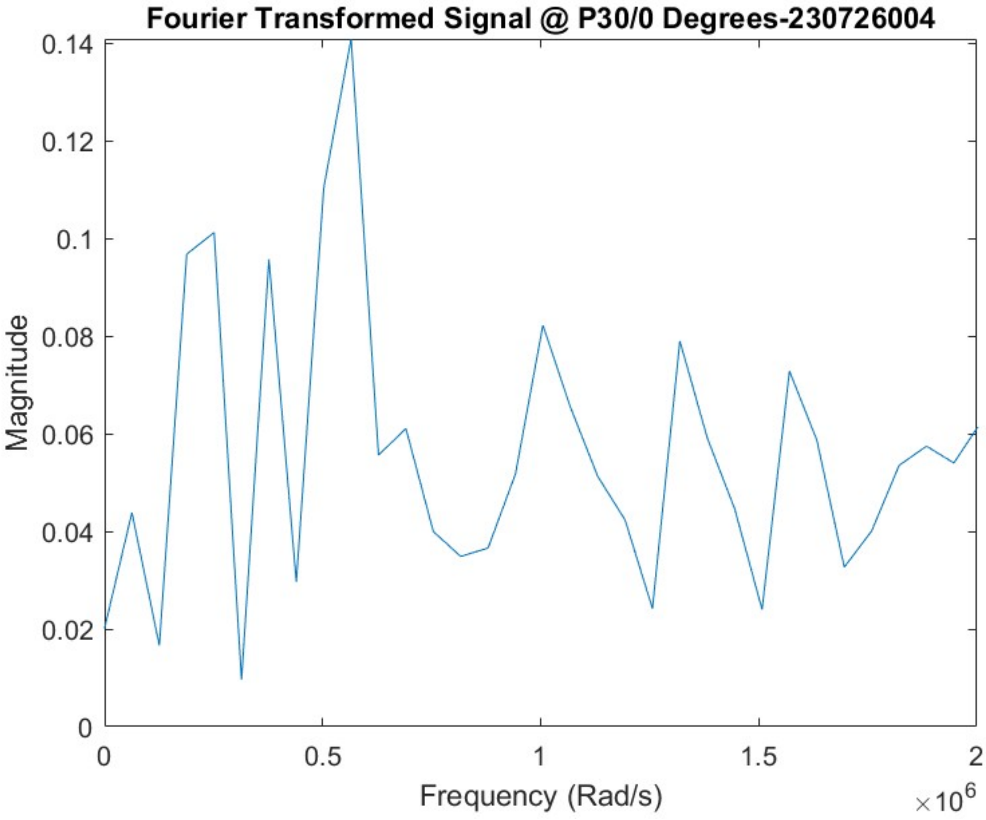

Figure 4.6: In this figure, the magnetic field data at P30 and 0 degrees is inputted into the *FFT* fast Fourier transform function in MATLAB to output a frequency range at this probe location. This result was then compared with the cross-correlation result to corroborate the findings found that showed the discrepancy with the predictive model for slow mangetosonic waves.

Chapter 5

INVESTIGATING ADJUSTMENTS TO THE MODEL

5.1 Overview and Non-Quantified Adjustments

With the discrepancy between the foundational predictive work and the frequency analysis work done afterwards, it is important to look at possible remedies that will strengthen the accuracy of the model and bring it in line with the frequency analysis. There are a few solutions explored with quantified results in this chapter but the first suggestion will be purely explanatory: that being the sub-spectral overlap caused by strong radial inhomogeneities mentioned prior. In this circumstance, the main continuous sub-spectral regions (like for the Alfvén and slow magnetosonic waves) will start to cross over each other leading to wave interference that may suppress higher frequencies or strengthen lower frequencies [8]. Another potential issue is related to effects from resonant wave interactions that are hard to encapsulate with just the Hain-Lüst model used in this research. Some of these types of interactions are discussed within the future work section.

5.2 Ampere's Law Approximation Adjustment

The first solution suggestion with a quantified result of the adjustment is the case of the magnetic field profile. With the approximation of Ampere's Law for the inside of the plasma ($B_2/B_1 = r_2/r_1$), the choice of a linear gradient and uniform current density may have oversimplified the radial behavior of the magnetic field and caused this prediction error. To test the effect of a deviation from the linear approximation, an arbitrary adjustment was made so that the field strength would decrease at a proportional rate of $r^{1.5}$. It was found that the magnetic profile approximation did not need to be changed significantly from a linear scaling to cause noticeable alterations to the way the Alfvén frequency would appear compared to the original model as shown in Figure 5.1. This adjusted Alfvén frequency set is closer to the results from the frequency analysis.

5.3 Pressure and Density Profile Adjustment

The density and pressure profiles was also adjusted to find a potential solution. The original profiles followed a quadratic scaling as shown by Eq. 3.40 and 3.41. To try and emphasize a shift as much as possible, an arbitrary profile proportional to $1/r^6$ was chosen. Despite this much faster profile scaling, deviations from the original quadratic approximations appeared to have a less noticeable effect on the outcome of the predictive model. In the case of the Alfvén sub-spectra frequencies, this can be explained partially by a weaker proportionality density has with the output as shown in Eq. 3.37. Also, the center and edge values for both the density and pressure remain unchanged which may have stopped the adjustment from having a more pronounced effect. The results of this adjustment are displayed for reference in Figure 5.2.

5.4 Doppler Shift and Velocity Profile Adjustment

Going into the effects of the Doppler shift caused by bulk plasma behavior, a change was first attempted through altering the wavenumber attached to the velocity profile. To emphasize this Doppler shift, the wavenumber was arbitrarily increased from k = 1 to k = 1000 and the effects can be shown in Figure 5.3. As with the density and pressure profile adjustments, despite the large shift of the wavenumber, the change is not noticeable with the outputted slow magnetosonic frequencies staying close to their original predictions of around 10^7 and 10^8 rad/s. Another issue arises from the fact that the Doppler shift is a linear transformation of the frequency. This can lead to shifted frequencies appearing below zero which is not a valid measurement for a temporal angular frequency. It is technically possible to just strengthen the wavenumber until the Doppler shift pushes the model and frequency analysis results into alignment but this would cause many frequencies to output

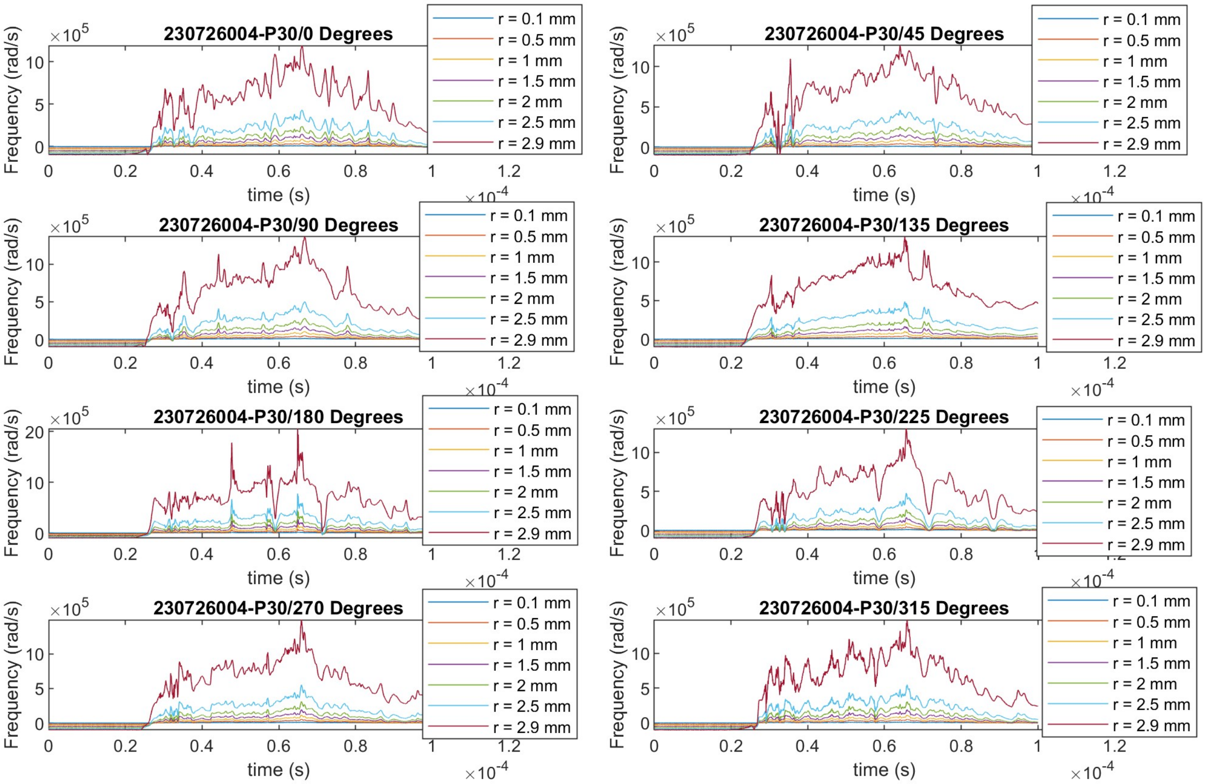

Figure 5.1: In this figure, the Alfvén sub-spectra is modified from the initial Ampere's Law profile approximation to the deviated faster scaling relation ship of $B \propto r^{1.5}$. This change to the radial magnetic field behavior causes a sizable shift from the original predicted results and lowers them by a factor of about 100.

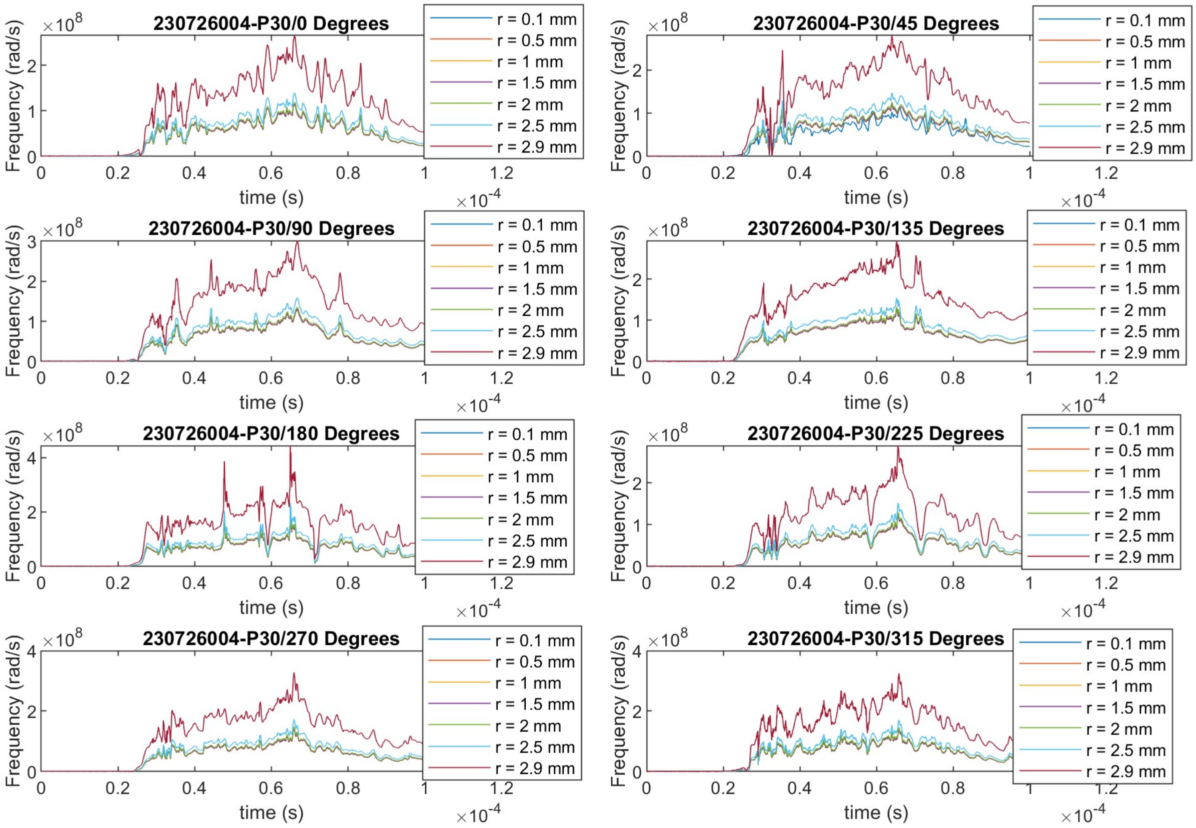

Figure 5.2: In this figure, the density profile was increased to as high as a $\rho \propto 1/r^6$ drop-off in order to emphasize the effect it would have on the model. Ultimately, it was a small change when comparing it to the effect of the magnetic field profile adjustment with the outputted frequencies being in the same 10^7 and 10^8 rad/s range as the original prediction. This was performed on the Alfvén sub-spectra.

negative. The other modification of the Doppler shift that was attempted is a change to the velocity profile itself. As stated before, the original velocity profile was linear moving at a gradient from 0 km/s at the center to 100 km/s at the surface of the plasma. Instead of this original profile, a velocity gradient more proportional to the shape $v \propto \sqrt{r}$ was arbitrarily chosen. This was done to accentuate Doppler shifts at some of the radial points within the plasma by using a much slower scaling velocity. The results of this modification are shown in Figure 5.4. What is shown is yet again a change with limited results as the altered slow magnetosonic frequency appear in the original range of between 10^7 an 10^8 rad/s. This outcome is partially explained by the same issue that came from the density and pressure adjustments. As in those cases, the velocity at the center and surface of the plasma were unchanged which can limit how strongly this shift can impact the actual magnitude of the velocity profile and therefore Doppler shift.

5.5 Adjustment Summary and Best Solution Suggestion

Based off of the work done to find solutions for the error between the predictive model and the frequency analysis, there only exists one adjustment that had a pronounced effect. With the density profile, pressure profile, Doppler shift wavenumber, and plasma velocity profile all having minor effects when shifted, only the Ampere's Law approximation adjustment appeared to make the model approach the results of the frequency analysis. However, despite this proving to be the closest finding to a solution for the error, it can't be taken with full certainty yet. The adjustment done for this research was arbitrary in order to emphasize how far the model would shift and lacked precision to find a final conclusion. Also, the current density profile within the plasma was assumed to be uniform and not actually known during this research. It would need to be included to get a more accurate picture of the magnetic field behavior within ZaP-HD for making a better approximation.

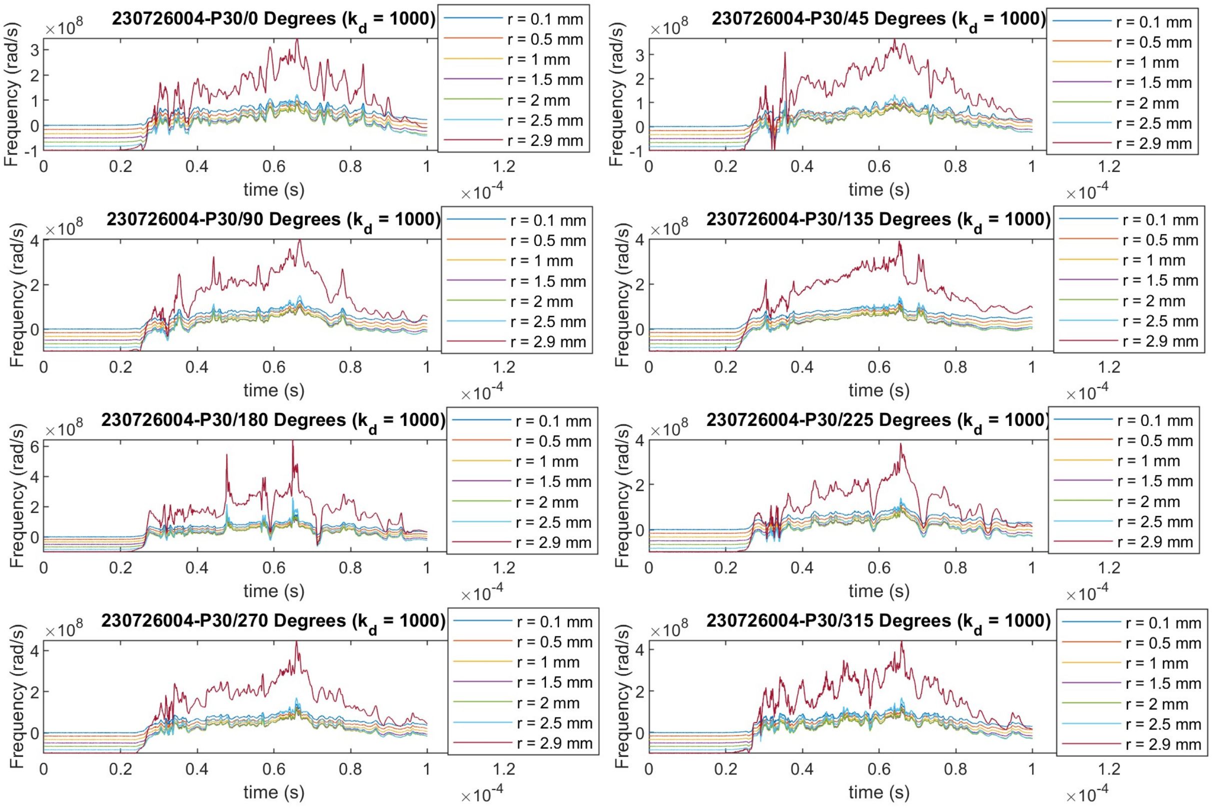

Figure 5.3: In this figure, wavenumber multiplied by the velocity profile at the given radial location within the plasma is amplified from k = 1 to k = 1000. This change is done on the slow magnetosonic sub-spectra. The change is not easily noticed with the frequencies appearing in the same range as the original predictions. There is also the issue of having negative frequency values that don't make sense physically.

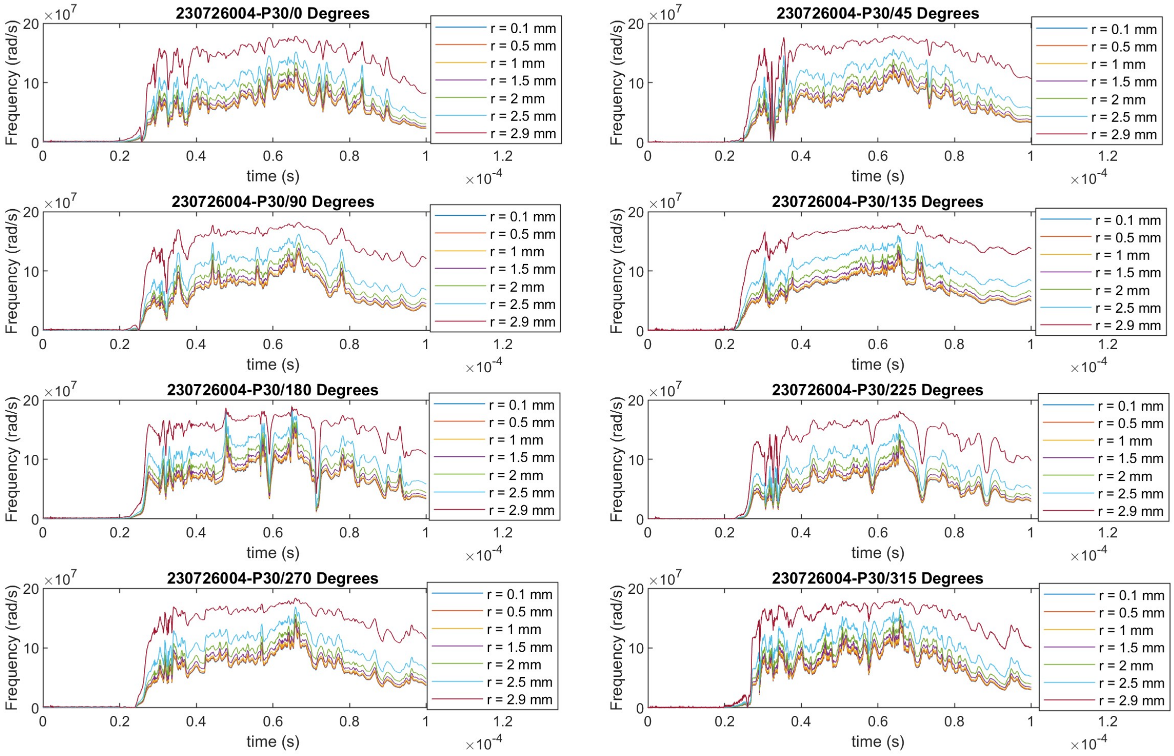
230726004-P30/0 Degrees

230726004-P30/45 Degrees

230726004-P30/90 Degrees

230726004-P30/135 Degrees

230726004-P30/180 Degrees

230726004-P30/225 Degrees

230726004-P30/270 Degrees

230726004-P30/315 Degrees

Figure 5.4: In this figure, the velocity profile is modified from its original linear profile to a square root relationship. This was performed on the slow magnetosonic sub-spectra. The effects of this alteration to the shape of the velocity gradient are small with the original 10^7 to 10^8 rad/s range of frequencies appearing. This can be explained partially by the limit of a shift in the velocity profile that doesn't change the magnitudes of center or surface values.

Chapter 6

CONCLUSION

6.1 Research Summary

The results of this research have proven that more work needs to be done to improve the accuracy of the MHD prediction model beyond the Hain-Lüst singularities combined with the radial profiles based off experimental data like the magnetic field, density, pressure, and flow velocity. The initial prediction that the Alfvén and slow magnetosonic frequencies were between 10^7 and 10^8 rad/s within ZaP-HD did not match the cross-correlation and Fourier transfrom results of the magnetic field periodicity data. These frequency analysis results, around 10^6 rad/s and potentially lower depending on the inclusion of outliers in the averaged range, illuminates a noticeable error that must be resolved in order for the model to have validity going forward to other frequency ranges outside of the MHD region. There are possible paths forward to align the two methods with the linear Ampere's Law approximation seeing the biggest change when deviated to a faster scaling profile, but it cannot be decided for certain and requires more research to refine fully.

6.2 Future Work

In order to fully finish this iteration of the MHD predictive model, the discrepancies between the frequency analysis and predictive model based off Hain-Lüst singularities need to be closed. This will involve taking the progress reached so far with the adjustments and then push further beyond the arbitrary suggestions made so far. To do this, more accurate measurements of other physical parameters for ZaP-HD like current density, plasma sheared flow velocity profile, pressure, and density need to be acquired and used alongside the magnetic field probe data used so far in this iteration. It will allow more robust physicalized profiles to be developed that more accurately depict plasma behavior than the idealized mathematical forms used for this research so far. Once this alignment between the model and the frequency analysis is achieved, the next iterations will involve moving beyond the MHD range and introducing instabilities. For example, other regions of the spectrum will be looked at and incorporated that specifically approach the higher frequencies and energies where particle involvement and statistical mechanics are important. Interactions that plasma particles have with the wave spectrum build from fundamental relationships shown mathematically by the Boltzmann equation,

$$\frac{\partial f}{\partial t} + \mathbf{v} \cdot \nabla f + \frac{q}{m} \left(\mathbf{E} + \mathbf{v} \times \mathbf{B} \right) \cdot \nabla_v f = \left(\frac{\partial f}{\partial t} \right)_{coll} \tag{6.1}$$

where f represents the particle distribution, **E** the electric field vector, **B** the magnetic field vector, q the electric charge, m the species mass, and **v** the particle velocity vector. This synergy between particles and waves can lead to circumstances like Landau damping that funnel energy into a wave mode and that can eventually lead to instabilities. It will be important to include behavior like this to make the model as well-rounded as possible. A much further goal after the complete realization of the full plasma wave spectral model would involve the application towards practical use within a device like ZaP-HD or other fusion devices for studying phenomena like Alfvén heating and radiation transmission mentioned at the beginning of this work.

BIBLIOGRAPHY

[1] Saied Goudarzi and Amir Raeisdana. Computation of Mass Sweeping Efficiency Factor and Current Efficiency Factor in Z-pinch Devices. *Journal of Fusion Energy*, 30(02):130–132, April 2011. `https://doi.org/10.1007/s10894-010-9341-8`.

[2] S. L. Jackson, U. Shumlak, B. A. Nelson, R. P. Golingo, R. C. Lilly, and T. L. Shreve. Effects of Initial Gas Injection on the Behavior of a Sheared-Flow Z-Pinch. *AIAA*, 2005. `https://doi.org/10.2514/6.2005-3853`.

[3] Michael Patrick Ross. *Exploring plasma stability and confinement with high resolution density measurements on the ZaP-HD Flow Z-Pinch*. PhD thesis, University of Washington, 2016. https://digital.lib.washington.edu/researchworks/items/6707a19a-82a5-477a-a1af-e7321b65c3a9.

[4] Y. Zhang, U. Shumlak, B.A. Nelson, R.P. Golingo, T.R. Weber, A.D. Stepanov, E.L. Claveau, E.G. Forbes, Z.T. Draper, J.M. Mitrani, H.S. McLean, K.K. Tummel, D.P. Higginson, and C.M. Cooper. Sustained Neutron Production from a Sheared-Flow Stabilized *Z* Pinch. *Physical Review Letters*, 122, 2019. `https://doi.org/10.1103/PhysRevLett.122.135001`.

[5] U. Shumlak, R. Lilly, C. Adams, R. Golingo, S. Jackson, S. Knecht, and B. Nelson. Advanced space propulsion based on the flow-stabilized z-pinch fusion concept. *AIAA*, 2006. `https://doi.org/10.2514/6.2006-4805`.

[6] Sina Taheri. *Time-discretization of a plasma-neutral MHD model with a semi-implicit leapfrog algorithm*. PhD thesis, University of Washington, 2021.

https://digital.lib.washington.edu/researchworks/items/633d90c9-e81a-401c-b54e-61685bfc5f0f.

[7] Sina Taheri, Jacob King, and Uri Shumlak. Time-discretization of a plasma-neutral MHD model with a semi-implicit leapfrog algorithm. *Computer Physics Communications*, 2022. `https://doi.org/10.1016/j.cpc.2022.108288`.

[8] Hans Peter Goedbloed and Stefaan Poedts. *Principles of Magnetohydrodynamics*. Cambridge University Press, 2004.

[9] James A. Mahaffey. *The History of Nuclear Power*. Facts On File, Inc, 132 West 31st Street New York NY 10001, 2011.

[10] Stewart C. Prager. Nuclear Fusion Power – An Overview of History, Present and futures. *International Journal of Advanced Network, Monitoring and Controls*, 04(04), 2019. `https://doi.org/10.21307/ijanmc-2019-064`.

[11] Bennett Diamond. Spatio-temporally Resolved Magnetic Field Measurements in the ZaP-HD Flow Z-Pinch Device Using Zeeman Splitting. Master's thesis, University of Washington, 2022. https://digital.lib.washington.edu/researchworks/items/f287d99e-1f04-4e1e-8cf9-57700a5d3dc6.

[12] Mary Ann Sweeney. History of Z-Pinch Research in the U.S. *Dense Z-Pinches: 5th International Conference on Dense Z-Pinches*, 2002. `https://doi.org/10.1063/1.1531271`.

[13] Uri Shumlak. Z-pinch Fusion. *Journal of Applied Physics*, 127(20), 2020. `https://doi.org/10.1063/5.0004228`.

[14] U. Shumlak, B.A. Nelson, E.L. Claveau, E.G. Forbes, R.P. Golingo, M.C. Hughes, R.J. Oberto, M.P. Ross, and T.R. Weber. Increasing Plasma Parameters Using Sheared Flow Stabilization of a Z-pinch. *Physics of Plasmas*, 24(5), 2017. `https://doi.org/10.1063/1.4977468`.

[15] Uri Shumlak and C.W. Hartman. Sheared Flow Stabilization of the m = 1 Kink Mode in Z Pinches. *Physical Review Letters*, 75(18), 1995. `https://doi.org/10.1103/PhysRevLett.75.3285`.

[16] B. B. Kadomtsev. *Plasma Turbulence.* Academic Press Inc, 111 Fifth Avenue New York, New York 10003, 1964.

[17] Eleanor Forbes. *Diagnostic Development and Plasma-Material Interaction Studies on the ZaP-HD Device.* PhD thesis, University of Washington, 2020. https://digital.lib.washington.edu/researchworks/items/2c70c559-cb36-4568-b259-79361847f150.

[18] D Gary Swanson. *Plasma Waves, 2nd Edition.* Institute of Physics Publishing, 2003.

[19] Raymond Golingo. *Formation of a Sheared Flow Z-Pinch.* PhD thesis, University of Washington, 2003.

[20] R.P. Golingo, U. Shumlak, and B. A. Nelson. Formation of a Sheared Flow Z-Pinch. *Physics of Plasmas*, 12, 2005. `https://doi.org/10.1063/1.1928249`.

[21] Sean Knecht. *Comparison of Electrode Configurations on ZaP: Investigation of Heating Mechanisms in a Flow Z-Pinch.* PhD thesis, University of Washington, 2012. https://digital.lib.washington.edu/researchworks/items/aa202ff2-c83c-4cad-ad8b-6cf9d13389b5.

[22] S.D. Knecht, R.P. Golingo, B.A. Nelson, and U. Shumlak. Calculation of the Equilibrium Evolution of the ZaP Flow Z -Pinch Using a Four-Chord Interferometer. *IEEE Transactions on Plasma Science*, 43(08):2469–2479, August 2015. `https://doi.org/10.1109/TPS.2015.2431973`.

[23] R.P. Golingo. Modeling magnetic fields measured by surface probes embedded in a cylindrical flux conserver. *Review of Scientific Instruments*, 78(03), March 2007. `https://doi.org/10.1063/1.2713435`.

[24] James M. Mitrani, Drew P. Higginson, Zack T. Draper, Jonathan Morrell, Lee A. Bernstein, Elliot L. Claveau, Christopher M. Cooper, Eleanor G. Forbes, Ray P. Golingo, Brian A. Nelson, Andrea E. Schmidt, Anton D. Stepanov, Tobin R. Weber, Yue Zhang, Harry S. McLean, and Uri Shumlak. Measurements of temporally- and spatially-resolved neutron production in a sheared-flow stabilized Z-pinch. *Nuclear Instruments and Methods in Physics Research Section A: Accelerators, Spectrometers, Detectors and Associated Equipment*, 2019. `https://doi.org/10.1016/j.nima.2019.162764`.

[25] V. E. Haloulakos and R. F. Bourque. Fusion propulsion study. Technical report, Astronautics Laboratory (AFSC), 1989.

[26] Jeff Peachman. Direct Energy Conversion From Flow Z-Pinch Exhaust Plume. Master's thesis, University of Washington, 2024. https://www.proquest.com/dissertations-theses/direct-energy-conversion-flow-z-pinch-exhaust/docview/3081566654/se-2?accountid=14784.

[27] Jared Smythe. Electrode Geometry Effects on Plume Characteristics and Thruster Performance of ZaP-HD. Master's thesis, University of Washington, 2023. https://digital.lib.washington.edu/researchworks/items/9416f421-e36e-4006-b4ce-c771f54fc0ee.

[28] U. Shumlak, C.S. Adams, J.M. Blakely, B.-J. Chan, R.P. Golingo, S.D. Knecht, B.A. Nelson, R.J. Oberto, M.R. Sybouts, and G.V. Vogman. Equlibrium, Flow Shear and Stability Measurements in the Z-pinch. *Nuclear Fusion*, 49(7), 2009. `https://doi.org/10.1088/0029-5515/49/7/075039`.

[29] John R. Buck, Michael M. Daniel, and Andrew C. Singer. *Computer Explorations in Signals and Systems Using MATLAB®, 2nd Edition.* Prentice Hall, Upper Saddle River, NJ, 2002.

[30] Petre Stoica and Randolph Moses. *Spectral Analysis of Signals.* Prentice Hall, Upper Saddle River, NJ, 2005.